Planetary Ephemerides Generation From Interplanetary Laser Ranging Data

H.R Abdolhay

Technische Universiteit Delft

TU Delft

Planetary ephemerides generation from interplanetary laser ranging data

by

H.R. Abdolhay

to obtain the degree of Master of Science
at the Delft University of Technology,
to be defended publicly on Tuesday August 22 , 2018.

Student number: 4301544
Project duration: December 11, 2017 – June 15, 2018
Thesis supervisor: Dr. ir. D. Dirkx, TU Delft

Cover Image: https://www.deviantart.com/breath-art/art/solar-system-for-print-605554295

TU Delft

"There is perhaps no better a demonstration of the folly of human conceits than this distant image of our tiny world"

Carl Sagan

Preface

This thesis treats the influence of interplanetary laser ranging on improving the planetary ephemerides. This study has been conducted by Hamid Reza Abdolhay, a master student of Aerospace Engineering, for Delft's University of Technology. This is the result of nearly 7 months of work that I have performed under the supervision of Dominic Dirkx.

I would like to thank Dr. Dominic Dirkx for supervising this interesting thesis, for his professional guidance and for giving constructive criticism during my work. I am also grateful to his valuable advice and steering me in the right direction during the software development part of this thesis. It has been of great value to this work.

My gratitude also goes to Delft University of Technology and its staff members for making this whole thesis possible. It created an educative opportunity to let me experience what working in a professional and challenging environment is about. It allowed me to develop my talents and explore my capabilities beyond boundaries.

Finally, I would like to thank my family for always supporting me and putting me in the right direction in life, giving their maximum effort for me to grow as an individual. Without them I would never be able to be where I am and who I am today.

Hamid Reza Abdolhay
Delft, July 2018

DELFT UNIVERSITY OF TECHNOLOGY

Abstract

Aerospace Faculty
Department of Space flight

by Hamid Reza Abdolhay

With the introduction of Interplanetary Laser Ranging (ILR), the acquired tracking measurements accuracy of planets can be improved drastically (up to a few millimeters (Dirkx, 2015)) which can result in an improvement in planetary ephemerides of not only the planet which is the target of laser ranging but also other bodies in the solar system due to dynamical coupling between the bodies. A quantitative analysis is performed to analyze how much improvement in the current planetary ephemerides can be achieved if highly accurate laser ranging observation were to be introduced in the current planetary ephemerides generation processes. The thesis achieved this by developing an ephemerides generation model using TU Delft's Astrodynamic Toolkit (i.e TUDAT) in which planetary ephemerides are generated for two cases. Once using simulated laser ranging observations to Mars between 2020 and 2023 and once without utilizing laser ranging observations. By comparing the estimated planetary ephemerides of the two cases, it is concluded that laser ranging to Mars resulted in a more stable and close to a factor of two improvement in ephemerides uncertainty for most of planets. The ephemerides of the Mars itself sees nearly a factor of ten improvement in uncertainty which resulted in a significant improvement in the knowledge of asteroid masses. The estimated mass parameter of 11 of the most perturbing asteroids in the solar system see more than a factor of ten improvement in their uncertainty which is unprecedented. Laser ranging to Mars and its cascade effect on the orbit of Mercury resulted in providing better constraints on PPN parameter γ and Sun's oblateness parameter J_2 allowing γ to be determined with an uncertainty of 5.5 $\times 10^{-8}$ which is 3 order of magnitude better than the constraints provided from Cassini experiment (Kopeikin et al., 2007). An order of magnitude improvement is also observed is Sun's J_2 parameter estimating it to an uncertainty level of 2.0 $\times 10^{-9}$.

Contents

List of Figures

List of Tables

Chapter 1

Introduction

1.1 Background Information

Currently, radio measurements and optical astrometry are the primary tracking data of solar system bodies which are then used to generate planetary ephemerides (Fienga et al., 2011). The state of art ephemerides generation processes, namely JPL's DE model (Folkner et al., 2014) and IMCCE's INPOP ephemerides solutions (Fienga et al., 2011), make use of all the different types of planetary observations that have been recorded throughout the history provides so in combination with the dynamical models of the solar system bodies to estimate the states of the solar system bodies. Table 3.1 provides a summary of many of the historical missions and observation data types that have been used up until now in state of the art ephemerides generation models. The dynamical models used in state of the art ephemerides generation process are mathematical representation of the actual dynamics of the solar system and they include various relativistic accelerations, additional perturbation forces due to non-homogeneous gravity field of the bodies, the tidal interaction in Earth-Moon system and finally they include nearly 343 asteroids in the simulation (which accounts for nearly 90 % of the mass of the asteroid belt) which is the case for JPL's latest ephemerides generation mode, DE431 (Folkner et al., 2014).

The state of art ephemerides generation models do not solely estimate the ephemerides but also a number of additional physical parameters (e.g mass of the asteroids in the asteroid belt) to simultaneously improve the uncertain parameters in the model while estimating the ephemerides. The ephemerides provided by DE and INPOP are used as an input in other fields of studies such as conducting relativistic experiments, designing future space missions etc Pitjeva (2013). Hence constantly improving their accuracy is of utmost importance in other scientific fields.

With the introduction of Interplanetary Laser Ranging (ILR), the acquired tracking

measurements accuracy can be improved drastically (up to a few millimeters (Dirkx, 2015)) which can result in an improvement in planetary ephemerides.

ILR operating principle is to some extend similar to radio ranging systems. There is a transmitter system which produces a laser beam at wavelengths of 532 (or 880 and 1064) nanometer with each pulse length being somewhere between 10 to 100 picoseconds. The detection system at the space segment triggers a tagging signal upon successful reception of the transmitted photons and the timing system tags the reception time using using a very accurate on board clock. Upon detection, the laser pulses are re-transmitted back to the ground segment to complete the ILR link.
There are a number of factors influencing the precision and accuracy of the ILR which are very briefly touched upon here. Instability of the clock's oscillator as well as clock biases can result in both stochastic and systematic noise on ILR measurements. For instance, Clocks that use hydrogen frequency standards can achieve very high stability which results clock noise errors of less than a millimeter for light time duration of 1000 seconds (Bauer et al., 2016). Moreover, delays in tagging the reception times and having non-calibrated hardware components on both ground and space segment are also among the sources of having biased LR observations which with proper calibrations and using state of the art hardware systems, these uncertainties are expected to be at 1 (Exertier et al., 2006). Environmental errors such as atmospheric turbulence results in random variations in the optical path length of the transmitted signal. The refraction of the signal as its propagating through different atmospheric mediums also results in systematic propagation delays and errors. The atmospheric turbulence can result in sub millimeter measurement noise (Kral et al., 2005) while the propagation delays can result in a few millimeter error by utilizing ray tracing method to correct for these delays (Hulley and Pavlis, 2007).

All of the above source results in a having few millimeter level accuracy for laser ranging, however having millimeter level observation accuracy for one planet does not translate into millimeter level accuracy for that planet's ephemerides. This is because of inconsistencies in our knowledge of solar system bodies' state. For instance, one planet that has an ILR link can have tracking data with millimeter level accuracy while other planets that have radio and radar tracking data have observation accuracy ranging from meters to kilometers respectively. Ultimately, this can diminish the achievable accuracy of the ephemerides of the planet with ILR link due to dynamical coupling between bodies in the solar system.

The above statement can also be reversed. Meaning, if a very accurate ILR observation link to one planet exists, then it can improve the accuracy of bodies ephemerides that do not have a very accurate observation link by utilizing the existing dynamical coupling between solar system bodies. To the date of this thesis, There have been no quantitative analysis performed to investigate how much improvement can really be achieved if an

ILR link was to be introduced to a planet in solar system. This provides the basis of conducting this thesis which its relevance, goals, motivations and layout are provided in the upcoming Sections.

1.2 Thesis relevance, motivation & objective

To this date, none have conducted a quantitative study to determine the level of improvement that one can achieve in planetary ephemerides if an ILR system was to be implemented. There have been studies where possible influences of ILR on specific cases have been analyzed, for instance utilizing ILR for better understanding of Martian system Dirkx et al. (2014), but none of them have done a comprehensive study for the effect of ILR on all planetary ephemerides in a full scale solar system simulation. Even though laser ranging is not yet realized in any actual mission over interplanetary distances, it can be expected to be utilized in the future missions as it has very high potential and its feasibility is already tested on a number of occasions. For instance, the scientific returns of Lunar laser ranging experiment, not only showcases the high potential of laser ranging and its contribution to scientific body, but also it has provided great inputs in reducing the technological gap in realizing ILR Williams et al. (2004). The highly accurate laser ranging observations to Moon are used in the state of the art ephemerides generation models and have resulted in a much better understanding of Earth-Moon system (Dickey et al., 1994) and relativistic gravity (Williams et al., 2004).

Moreover, number of tests have already been performed in the past to prove the ILR feasibility. For instance, in 2004, laser pulses were sent to MESSENGER satellite which was on its way to Mercury and the laser altimeter on board of MESSENGER (Cavanaugh et al., 2007) also transmitted some laser pulses to ground station (Smith et al., 2006), successfully completing a two-way ILR link. In this mission, proper time tagging has been performed which provided range measurements with uncertainties of about 20 centimeter. Even though the satellite's hardware was not designed specifically for ILR, it managed to provide highly accurate range measurements. Mars Global Surveyor detected laser pulses from ground resulting in an improvement in on board clock of this surveyor by detecting a 10 millisecond offset on its clock (Neumann et al., 2006). As studies have already proven ILR feasibility and proposed ways to implement them in future missions (Dirkx, 2015), expecting ILR to be operational in near future is likely. Hence conducting an analysis on the effect of ILR on planetary ephemerides becomes very relevant, making the content of this thesis contributing to the current body of knowledge.

Therefore, on the basis of what was explained in the previous paragraphs, the main goal of this thesis can be established. The goal of the master thesis it to conduct a quantitative analysis to investigate how much improvement in the current planetary ephemerides can be achieved if highly accurate laser ranging observation were to be introduced in the current planetary ephemerides generation processes. The thesis aims to achieve this by generating planetary ephemerides using simulated laser ranging observations to a selected candidate planet. Then comparing the estimated planetary ephemerides with a set of planetary ephemerides that are generated without using simulated laser ranging observations. This comparison is done by looking that the errors of the both simulation results and quantify the improvement in planetary ephemerides errors.

The motivation for conducting this analysis is to ultimately improve the planetary ephemerides accuracy by utilizing ILR. The question of why having more and more accurate planetary ephemerides accuracy is important has a number of reasons which some of them are highlighted below. The planetary ephemerides provide important information in understanding the evolution of the solar system and its stability. Additionally, accurate ephemerides are used to observe relativistic effects (Xie and Deng, 2013). By accurately analyzing how ephemerides are affected due to relativity, one can also estimate relativistic parameters accurately which is an important science return of having accurate ephemerides. The accurate estimation of relativistic parameters not only allows one to further prove the theory of general relativity but also improve the accuracy of relativistic light-time correction applied to the observations, resulting in an improvement in overall accuracy of the range measurements. For instance, having accurate ephemerides allows for accurate observation of precession of planets orbits which is defined as the change in argument of pericenter of the planet's orbit in each orbital revolution due to relativistic effects. These accurate observations can be used to test various theories of relativity or constrain them (Wakker, 2015).

All in all, the main research question that is aimed to be answered in this thesis is given as follows.

How much improvement in planetary ephemerides uncertainty (or error) can be achieved by introducing interplanetary laser ranging observation in a planetary ephemerides generation process?

The above research question raises the following sub questions

- How much improvement in uncertainty can be achieved for the body where an ILR link is established?
- By establishing ILR to one body, how much improvement in uncertainty can be achieved for other bodies which no or very little observations are available?
- How effective is ILR for improving the mass parameter of the bodies in the asteroid belt?
- How much can ILR contribute in improving the relativistic parameters used in the ephemerides generation models?

It is important to note that the goal of this thesis is not to necessarily produce planetary ephemerides with absolute accuracy that can compete with the state of the art ephemerides. But it is to perform a study between two relative cases in order to analyze the potential of ILR.

Since the scope of this thesis is very broad and can have many possible follow-ups in the future, taking it into any direction, the simulation model that was developed for this thesis is decided to be designed in a sandbox fashion. Meaning that anyone interested into further exploring the possibilities of laser ranging can directly use the code produced for this thesis [1] and simply tamper with its input values to test any other desirable hypothesis. Hence the code that is produced in this thesis can be used as a framework that eliminates the need of having to recreate a new ephemerides generation model every time a similar study needs to be performed. It is also setup in such a way that with minimum to no knowledge of TUDAT or C++, one is sill able to use the simulation model.

[1] https://github.com/habdolhay/ILRMasterThesis

1.3 Thesis Layout

The layout of this thesis is as follows. Chapter 2 explains how the process of developing an ephemerides generation model and all provides all the required components. Section 2.1 of Chapter 2 opens up by first explaining how the model of the solar system in this thesis compares to reality, what assumptions come with it and how one can asses the errors of this model. Then in Section 2.2 all the bodies that are and are not necessary to include in an ephemerides generation are tackled. This is followed by Section 2.3 which specifically purposes a way of including the full effect of the asteroid belt in the ephemerides generation model both effectively and efficiently without spending too much computational budget. In Section 2.7, the mathematical representation of all the acceleration models that should exist in an ephemerides generation model is provided. Sections 2.4.2 and 2.6 explain how often and from which missions the required planetary tracking observations are generated as well as what appropriate noise level that put on top of them ensure the simulated observations represent the actual observations from real missions. Finally, Chapter 2 ends with Sections 2.9 which explains what parameters are estimated during the estimation to best answer the research question.

Chapter 3 validates all the choices and assumptions made in the ephemerides generation model given in Chapter 2 by performing a Known-Input Known-Output test and comparing its performance with performance of the state of the art ephemerides generation models.

After validation of the model is complete, Chapter 4 uses the developed model to conduct an analysis on the effect of ILR on planetary ephemerides by using the inputs that were introduced in Chapter 2. Chapter 4 displays in what ways ILR can improve the planetary ephemerides, the knowledge of asteroid belt as well as the knowledge of the dynamical parameters of the solar system and relativistic gravity.

Finally, Chapter 5 gives some remarks about the effect of laser ranging on planetary ephemerides as well as providing a definitive answer to the research question that were raised in Section 1.2. Chapter 5 ends with a recommendation which opens some ideas on how one can use the results and the model developed in this thesis to further explore the capabilities of laser ranging and recommends how one can further improve the results that were produced in this thesis.

Chapter 2

Simulation Setup

This Chapter is dedicated to describing the scope of the ephemerides generation model that is developed in this thesis using TU Delft's Astrodynamics Toolkit (i.e TUDAT) in order to produce ephemerides that can help answering the question and goal of the thesis provided in Section 1.2.
First, a top level view of the simulation model, the assumptions related to it and the criteria used to asses the performance of the estimation are explained in Section 2.1. Then in Section 2.2 and 2.3, all the bodies that are included in the simulation model as well as how the solar system asteroids are modeled and treated are explained. After all the bodies are established, the interplanetary missions to these bodies and their respective observation schedules are explained in Section 2.4.2. This followed by Sections 2.5and 2.6 which explain the observation models that are used to simulate different type of observations as well as the process of how and what noise levels are added to them to make them realistic. All the mathematical models that are used to set up the acceleration models are given in Section 2.7. In Section 2.8, the integration settings of the simulation is briefly explained and Finally in Section 2.9, explanations are provided on which parameters are estimated in this thesis to best answer the research question.

2.1 Reality vs Virtual Reality

In state of art ephemerides estimation processes, observations from actual missions to different planets are used in an estimation model which consists of a number of dynamical models that attempts to reenact the reality as closely as possible. The state of the art estimation models are not perfect due to errors in either the parameters that are used to describe the model, how the model is formulated and in the initial condition of the estimation. Moreover, the tracking observation themselves are not ideal and are inherently noisy as they carry errors that exist in reality. Clock biases, hardware errors, atmospheric delays etc all contribute to uncertainty of the available observations.

Consequently, the state of the art ephemerides generation processes estimate planetary ephemerides using a imperfect estimation model with noisy tracking observations. This means the outcome of the estimation model (i.e the estimated ephemerides) will contain a level of uncertainty that are due to these differences.

As was mentioned in Section 1.2, reproducing ephemerides that compete with state of the art ephemerides is not part of the scope of this thesis and it becomes very difficult to achieve. The first reason for complexity of reproducing the state of the art ephemerides is having very little accessibility to the actual tracking observations of planets as well as their actual uncertainty budgets. Even if all the observations were to be accessible, processing these observations and developing an estimation model that exactly reenact the state of the art estimation models would require a standalone research and extremely large computational budget to execute, in particular, treatment of asteroids realistically poses a computational bottleneck to this problem. As this thesis mainly focus on analyzing two hypothetical cases relative to one another which are not bound to any time frame, the need to have actual planetary observations becomes unnecessary. It then becomes much more beneficial to use simulated observations in order to perform this thesis which provides the most flexibility in terms of testing various hypothetical scenarios without having to be limited to actual observations. It allows for defining custom observation schedule and any desirable or future missions, experimenting with different observation noise levels etc. This level of freedom allows the model to be a framework for doing any further research without any limitations or reliance on real missions tracking data. In order to maintain consistency and avoid any erroneous estimation due to having observations from different sources, all observations are internally simulated by solving planetary state functions using TUDAT's built-in functionality. [1]

In order to simulate the observations, a virtual reality environment needs to be set up which should reenact what is happening in the actual solar system as accurately as possible. This virtual reality environment is used as the truth model meaning the ephemerides that are calculated in this environment are used as an ideal reference point to compare the estimation results to. The virtual reality is designed to represent the actual reality, as closely as possible, in which any user defined and hypothetical planetary missions, ground stations etc can exist. Next to this virtual reality environment, there is the estimation model which is an independent model designed to estimate the ephemerides that are produced in virtual reality using the simulated observation. This hierarchy is shown in Figure 2.1 which shows how the virtual reality and estimation model compares to reality and state of the art ephemerides generation models.

[1] http://tudat.tudelft.nl/tutorials/tudatFeatures/estimationSetup/observationSimulation.html

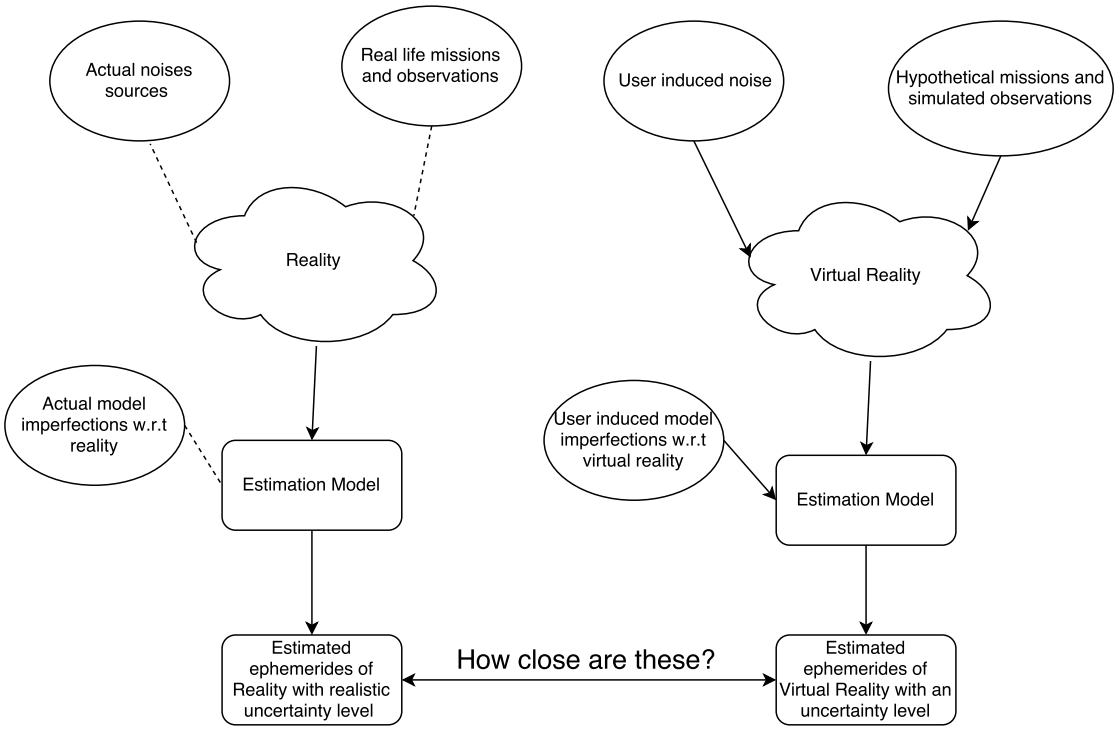

FIGURE 2.1: Figure showing the difference between the state of art ephemerides generation models(on the left) and the way the model is setup in this thesis(on the right)

As can be seen in the left diagram in Figure 2.1, the state of the art estimation models make use of real observations with real noise budgets in an attempt to estimate ephemerides in of the real solar system. On the other hand (as can be seen from diagram on the right and in more details, Figure 2.2), in this thesis first the virtual reality is simulated which computes all planetary ephemerides and simulate the necessary observations. Then another model is used in an attempt to estimate the ephemerides that been computed in virtual reality. It becomes clear that if the simulated observations were to have no noise and there were no differences in the dynamical models of the estimation model and the virtual reality, then the estimated ephemerides from the estimation model would perfectly resemble the ephemerides that were computed in the virtual reality. This is of course not realistic as it is important to ensure the differences between virtual reality and estimation model resembles the differences between actual reality and state of the art ephemerides generation models.

Consequently, one requires to induce the necessary differences between the virtual reality and estimation model (e.g difference in dynamics, add observation noise, etc) to ensure the whole system of this thesis becomes a good representation of reality. The main challenge is to apply a realistic noise level on the observation and a difference between the dynamical model of virtual reality and estimation model such that the outcome of the left system in Figure 2.1 matches or come close enough to the outcome of the right system in Figure 2.1. The estimated ephemerides do not necessarily need to be the same

for the two systems as long as their relative uncertainty is similar, the setup becomes a valid representation of reality. This is shown in Chapter 3.

The virtual reality environment attempts to represent the actual solar system dynamics as close as mathematically and computationally feasible. Throughout this Chapter, all the required components to setup the virtual reality environment as well as explaining the settings for the estimation model in order to answer the thesis question are explained.

2.1.1 Representation of true estimation error

Typically after parameter estimation process is performed, the diagonal elements of the computed covariance matrix of the estimation is used as a mean to get the uncertainty of the estimated parameters (as explained in Appendix C). Each element along the diagonal of the covariance matrix is the statistical variance of each of the estimated parameters. These variances are indicative of how well the estimated parameters were fitted to the available observations, providing an statistical overview of how confident the estimated parameters are. This uncertainty is referred to as the formal errors of the estimation. In orbit determination, the formal errors of the estimated parameters is believed to be optimistic. The true uncertainty can be up an order of magnitude larger (Lemoine et al., 2013), in orbit determination of spacecrafts, and it can be a factor of two to three larger when estimating planetary ephemerides (Folkner, 2010) depending on how well estimation and observation model is capable of reenacting reality (Folkner, 2010). Also these formal errors need to be propagated in time in order to given some information about the error evolution over time. This propagation is mainly done using linear schemes, though other and more complex and accurate schemes are available (Luo and Yang, 2017), which and are based on a number of assumptions which casts further shadows over reliability of formal errors as a means to define the uncertainty of the parameters. Therefore, purely looking at the formal error of the estimation is possible but does not provide the full picture of the actual uncertainty.

In this thesis, a virtual reality model is developed which acts as a truth model or reference model and there is an estimation model which attempts to estimate the truth model as closely as possible. Hence one can directly compare the results of the estimation model with the truth model in order to asses the performance of the estimation model and how well it can represent the truth model (as shown in Figure 2.2). This is a great alternative to formal error and eliminates the disadvantages of formal error and its propagation. This error is called true error and from now on in this thesis all the computed errors will represent the true error unless it is specified otherwise. The downside of this method is that the resulting true error becomes only one of the possible realizations of the uncertainty distribution and if one requires to get an uncertainty level, it needs to run the simulation multiple times with different initial conditions to get the

variance of the uncertainty distribution. It also requires to apply a proper difference between the estimation and the truth model to ensure the true error and its relation to formal errors is realistic.

Whether this way of representing the error is valid or not is tested and validated in Chapter 3 which checks how the true error compares the the state of the art planetary ephemerides formal errors.

2.1.2 Top level simulation diagram

A top level diagram of the simulation that is setup in this Chapter to perform the analysis is given in Figure 2.2. It is important to note that this is a very top level diagram of the simulation meaning it does not show every individual function and every single input and output parameter for each block. It is merely a representative of how the top level information flow through the simulation, as well as the general inputs and outputs of the simulation.

It can be seen from Figure 2.2 how virtual reality (i.e truth model) and the estimation model interact. For every block that is shown in the diagram, the corresponding Section of this thesis is stated in which the inputs and outputs of that block is thoroughly explained. This is used as a mean to give an idea of how information from different Sections of this thesis flow together. The text on the arrows indicate what information goes in and what is expected to come out of each block on a very top level.

It can be seen that there are two independent acceleration models for both estimation model and the truth model. This is done to given user freedom to induce any desirable differences between the two dynamical models in order to perform different analysis. In this thesis, the differences between truth and estimation environment are summarized as follows.
The acceleration models in both virtual reality and estimation model are identical with the only difference being in the parameters that are used to describe them. In the estimation model, The planets' states that are to be estimated are perturbed and the asteroids' masses that are to be estimated are also perturbed based on their currently known confidence level given in literature (Baer et al., 2011) (Konopliv et al., 2011) to see how the estimation retrieve the true values. The other and more important way that is used to impose differences between the virtual reality and the estimation environment is done by adding a realistic noise profile on the observation which are there to account for various error sources in observations and also unmodeled dynamical forces that are supposedly exists in truth model but are not accounted for in the estimation model. Section 2.6.1 illustrates how this noise profile is designed.

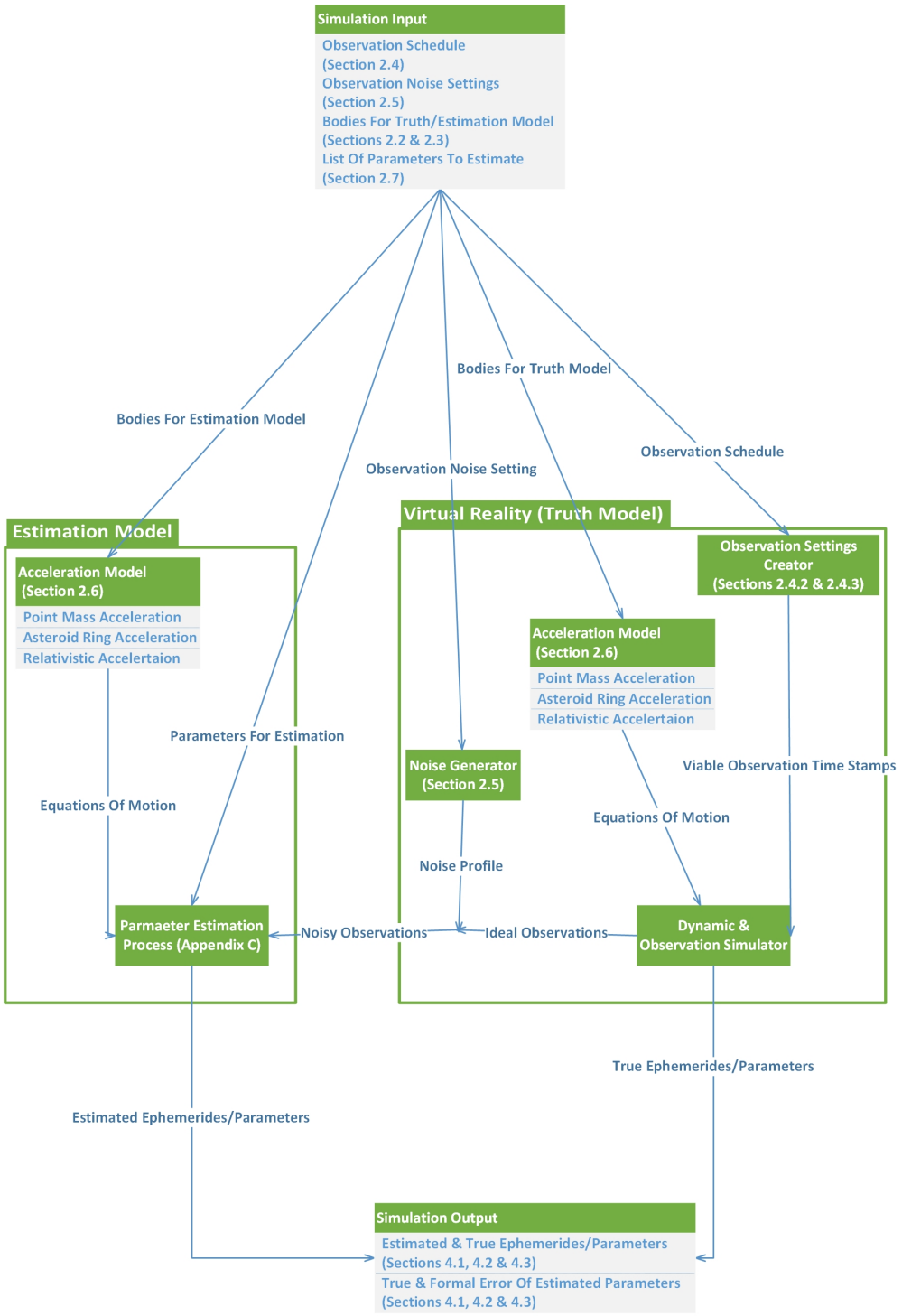

FIGURE 2.2: A top level simulation diagram displaying the logical flow of the information and their corresponding Sections. This diagram does not display all the functions nor all the inputs and outputs of the simulation but its merely a top level flowchart of information interaction

2.2 Major bodies in Virtual Reality & Estimation model

The virtual reality (i.e truth model) is modeled in such a way that it reenacts the actual solar system as closely as possible. Therefore, it requires to include all the major bodies in the solar system. Whether inclusion of the moons of all planets in the virtual reality environment is necessary or not, depends on the number of factors to consider which are explained as follows.

The Moons have a much smaller orbital period compared to the planets (e.g Galilean moons have orbital periods of between approximately 2 to 17 days). When one compares the Moons' orbital periods to the orbital period of the planets which range from about 90 days to more than 100 years, it becomes apparent that a very small integration step size would become required to accurately propagate their states. During the simulation, the selected integration step size is generally dominated by fastest moving objects and inclusion of moons can result in a very high computational effort and time, especially for simulation periods of multiple years. Moreover, the accumulated numerical errors of a fast moving object can become very large for long simulation periods which makes inclusion of moons a hindrance.

Computational effort alone is not the sole reason to consider neglecting the moons. There exists two other elements that should be examined. First one is how accurately the orbits of the Moons can be reconstructed in virtual reality model and the second one is how significant the mutual effect of the moons on their parent planets are (i.e in terms of how significant these effects are on the ephemerides of their parent planets). For instance, modeling the Jupiter's gravity field accurately is required to reconstructs orbits of the Galilean moons properly as that has a significant effect on their orbits. It was only recently that JUNO's Doppler tracking data allowed for an accurate determination of Jupiter's gravity field which is still limited to the JUNO's orbit geometry (Folkner et al., 2017). The gravity field of other gas giants are much less accurately known hence making reconstruction of their respective moon's orbit accurately challenging (Helled et al., 2010). Hence other than Earth's moon orbit which is highly accurately known due to lunar laser ranging and partially Galilean moons, other moons in the solar system are not very well constrained.

The second factor that was mentioned was the mutual effect of the moons on their parent planets in terms of how significant these effects are on the ephemerides of their parent planets. A simple analogy is made to provide a preliminary perspective on the significance of the moons' effect on their parent planets ephemerides using Table 2.1.

TABLE 2.1: List of some of the major moons and their relative Mass and Distance to their parent planets

Moon Comparison			
Parent Planet	*Moon name*	*Mass percentage of parent planet*	*Distance to parent planet -[km]*
Earth	Moon	1.2 %	384,000
Jupiter	Ganymade	0.008 %	1070,000
	Callisto	0.006 %	1882,000
	Io	0.005 %	422,000
	Europa	0.002 %	671,000
Saturn	Titan	0.024 %	1222,000
	Rhea	0.004 %	527,000
	Iapetus	0.003 %	3560,000
	Dione	0.0002 %	377,000
	Tethys	0.0001 %	294,000
Uranus	Titania	0.004 %	436,000
	Oberon	0.002 %	583,000
	Umbriel	0.001 %	266,000
	Ariel	0.002 %	190,000
Neptune	Triton	0.02 %	354,000

The interaction between Earth-Moon induces a wobble in Earth's orbit of a few kilometers which if neglected, will cause the Earth's orbit to behave differently which has a consequent effect on the orbit of inner planets due to dynamical coupling between them (Touma and Wisdom, 1994). The moons of gas giants have have much smaller mass compared to their parent planets which means the effect that those moons induce on their parents orbits becomes very small and investing the computational effort to account for those effect becomes superfluous. As can be seen from Table 2.1, Earth's Moon which is at a distance of 384,000 kilometers from Earth has a mass of about 1.2 % of Earth. Ganymede, the largest moon in the solar system, is at a distance of nearly 1 million kilometers from Jupiter and has mass of about 0.08 % of Jupiter's mass. This makes Ganymede effect (and other Galilean Moons following from same analogy) on Jupiter's motion extremely small compared to effect of the Earth's Moon on Earth. A similar analogy can be made for moons of other planets which is summarized in Table 2.1 that can be used to conclude that, other than Earth's Moon, including all other moons in the virtual reality and estimation model becomes unnecessary as they do not have any significant effect on the ephemerides of their parent planets (and other planets).

2.3 Treatment of Asteroids in Virtual Reality & Estimation model

The inclusion of the bodies in asteroids belts is important in the simulation. Asteroid belt has a significant effect on orbits of inner planets, especially Mars due to this planet being very close to the main asteroid belt (Standish Jr and Hellings, 1989). Inclusion of all asteroids in the virtual reality and estimating all of their individual mass parameters during estimation is not computationally feasible. Hence an alternative is suggested to be used for this thesis but first a review of how asteroids are treated in the state of the art ephemerides generation models is provided.

In the state of the art ephemerides generation models, the effect of the 343 asteroids that theoretically have non negligible effect on the orbit of the Mars are included in the dynamical models (Viswanathan et al., 2017) (Folkner et al., 2014). All of these asteroids are individually propagated and their mass parameters are individually estimated. The asteroid masses are initialized at the beginning of the estimation using their current best estimates and from the direct observations of their radius made by WISE Mission which are translated into mass parameter. [2]

The computational budget available for this thesis is not sufficient to treat the asteroids the same way as it is treated in state-of-the-art ephemerides generation models. Therefore, it is only computationally feasible to include a limited number of individual asteroids in the virtual reality and estimation model. An alternative option is to model the rest of the asteroids in the asteroid belt by a ring as is proposed by a (Kuchynka et al., 2010). The results of the study proves that for the ring model to be 99 % effective (i.e to account for 99 % percent of the effect of the total asteroid belt), a number of around 300 optimally selected asteroids need to be included individually in combination with having a ring model for the rest of the asteroids belt. This does not mean that the ring model becomes completely ineffective if one includes less than 300 individual asteroids though. The individually included asteroids are selected optimally selected in order to make the most out of the ring model and this selection is done by solving a Mixed Integer Quadratic Optimization Problem (MIQP) that selects which asteroids are optimal to include individually for ring model to be as effective as possible. This analysis is already performed by (Kuchynka et al., 2010) in which he proposes the optimal ring characteristic for any number of individually included asteroids. The results of this study are used as a basis for asteroid treatment in this thesis.

How the ring model and individual asteroids complement each other are explained using Figures 2.3 and 2.4 (taken from (Kuchynka et al., 2010)) which show the effect of including a ring model together with N number of individually included asteroids. Figure

[2] http://wise2.ipac.caltech.edu/docs/release/neowise/neowise_2018_release_intro.html

2.3 shows (in terms of percentage) the magnitude of the remaining perturbations that are not yet covered after fitting the ring model and including N asteroids individually. The dotted line represent the case where the selected N number asteroids are the most perturbing ones and the solid line shows when the N number of asteroids are selected optimally after solving the MIQP averaged over 100 runs.

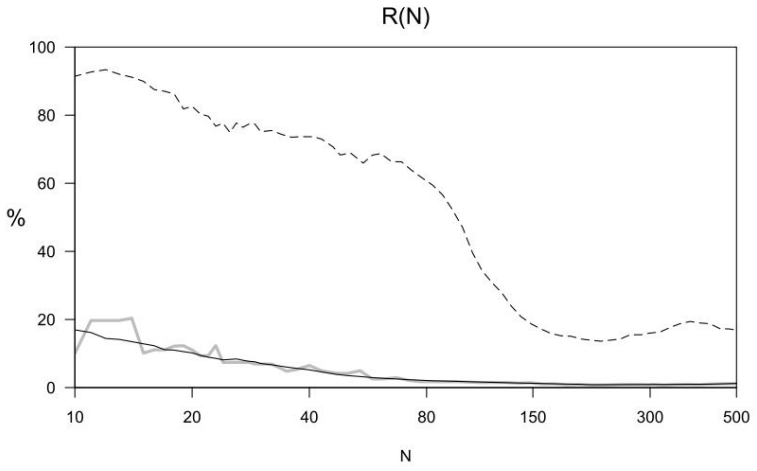

FIGURE 2.3: What portion of the remaining perturbation on Mars's orbit (in percentage) are not yet covered after including N asteroids individually in combination with an asteroid ring. The dotted line represent the case where the selected N number asteroids are the most perturbing ones and the solid line represent the case where the selected N number of asteroids based on solving MIQP averaged over 100 runs(i.e optimal asteroid selection). The gray line represent one of the 100 runs(Kuchynka et al., 2010)

The following example is provided on how to interpret Figure 2.3. For instance, If one was to include 10 of the most perturbing asteroids individually in the asteroid models in combination with an asteroid ring model, around 80 % of the remaining perturbation amplitude would still left to be covered. Figure 2.4 shows the same results but in terms of range uncertainty in Earth-Mercury (lines c and c'), Earth-Venus (lines b and b') and Earth-Mars (a and a'). This Figure indicates how much uncertainty will still be left in the orbits of Mercury, Venus and Mars after combining a ring model with N number of individual asteroids.

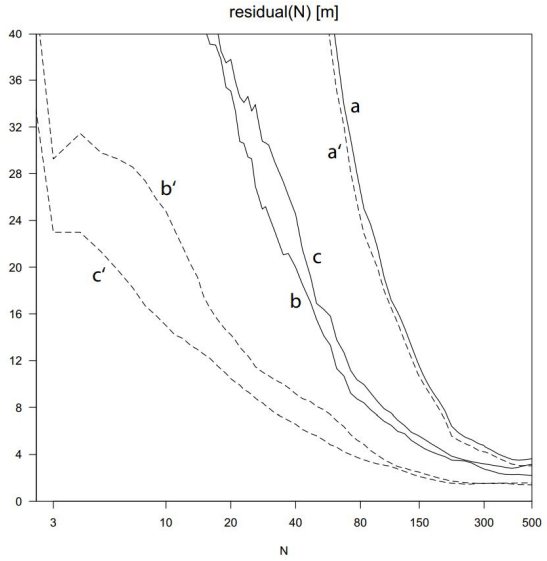

FIGURE 2.4: How much uncertainty will still be left in the orbits of Mercury (lines c and c'), Venus (lines b and b') and Mars (a and a') after combining a ring model with N number of individual asteroids (after 30 years of simulation). The dotted line represent the case where the selected N number asteroids are the most perturbing ones and the solid line represent the case where the selected N number of asteroids based on solving MIQP (i.e optimal asteroid selection)(Kuchynka et al., 2010)

For this thesis, results from Figures 2.3 and 2.4 are used as a reference point on choosing how many asteroids to include individually in the virtual reality and estimation model as well as the complementary ring's characteristics. Based on some preliminary tests, propagating more than 20 individual asteroids in virtual reality and estimation model is not computationally feasible as it uses well over 50 Gigabytes of memory that is available to conduct the thesis on but this value depends strongly on how long the simulation is run for. On average for a 30 year simulation time, only around 11 asteroids is computationally feasible to be included individually which requires 48 Gigabytes of memory. Hence it becomes apparent that including an asteroid ring in virtual reality would result in a drastic improvement in the modeling of the solar system asteroid belt. This would make it possible for the virtual reality environment to reenact reality to a much closer level. It would also be possible to completely exclude the ring and only include 11 asteroids in virtual reality which would significantly simplify the dynamical model of the virtual reality as the acceleration model of the ring does not need to be modeled anymore. But excluding the ring means a significant portion of the dynamical effect on the solar system bodies are being neglected. It is estimated that ring will have a lumped effect of a few kilometers on the orbit of Mars as also shown in Figure 2.5 which is best to be included to ensure the virtual reality model developed in this thesis reenact the actual solar system as closely as it can. .

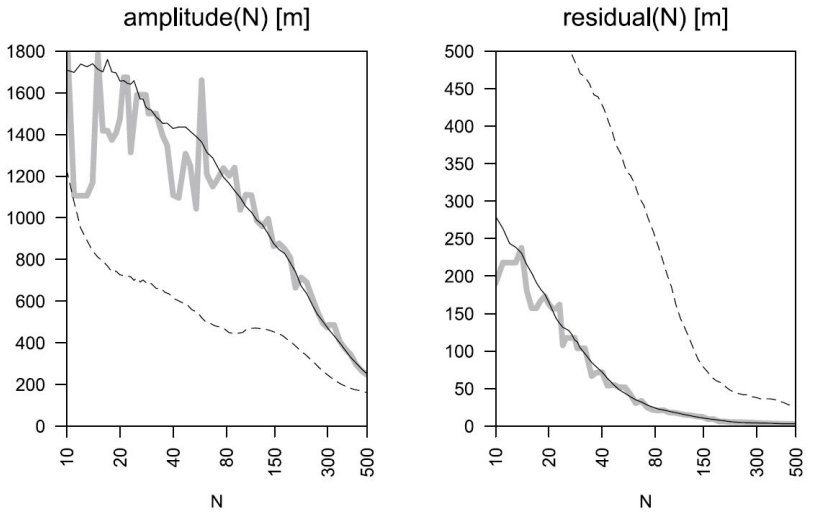

FIGURE 2.5: How much uncertainty will still be left in the orbits of Mars after combining a ring model with N number of individual asteroids (after 30 years of simulation). The dotted line represent the case where the selected N number asteroids are the most perturbing ones and the solid line represent the case where the selected N number of asteroids based on solving MIQP (i.e optimal asteroid selection) averaged over 100 runs. The gray line is one of the 100 runs. (Kuchynka et al., 2010)

2.3.1 Asteroids selection process

The question of which asteroids to include is already answered by (Kuchynka et al., 2010) which is based on solving MIQP using a Monte Carlo approach with 100 different runs. In all runs, a number of asteroids had a probability of 98 % - 100 % of being selected to be the optimum ones to include individually. Among these asteroids, a list of the 20 asteroids with an effect of higher than 100 meters on Mars's orbit (over 30 years) are provided in Table 2.2 along with their nominal mass parameter which is the current best estimate of these asteroid masses. These values are called nominal values (or true values) as they are used in the truth model to generate the true reference ephemerides. The masses themselves are also used as a reference to compare the estimated asteroid mass parameters to in order to see the relative improvement that one can achieve with laser ranging (see Section 4.2). The first 11 asteroids shown in Table 2.2 are included individually in virtual reality and their masses are estimated during the estimation as computationally, including more asteroids becomes unfeasible. These asteroids are complemented with a ring with characteristics shown in Section 2.3.2.

TABLE 2.2: List of 20 most optimum asteroids to include individually in Virtual Reality along side the ring model (ordered based on their mass parameter)

Asteroid Name	*Nominal* μ_{ast} $[km^3/s^2]$
1 Ceres	63.18
4 Vesta	17.74
2 Pallas	14.08
10 Hygiea	5.84
31 Euphrosyne	3.58
704 Intermanta	2.60
511 Davida	2.56
15 Eunomia	2.11
3 Juno	1.99
52 Europa	1.75
48 Doris	1.73
16 Psyche	1.52
532 Herculina	1.15
29 Amphitrite	1.03
9 Metis	0.98
7 Iris	0.97
6 Hebe	0.83
324 Bamberga	0.75
19 Fortuna	0.55
24 Themis	0.53

2.3.2 Modeling the asteroid belt as a ring

The theory behind modeling the asteroid belt as a ring is directly based on the analysis performed by (Kuchynka et al., 2010) which assumes the ring has a fixed radius of 2.8 AU and is treated as an object with its center is at barycenter of the solar system coinciding with the ecliptic plane. Both mass and radius of the ring can be adjusted depending on how many asteroids are to be included individually, but as also shown in analysis done by (Kuchynka et al., 2010), its simpler to fix one of the parameters (e.g ring radius) and only adjust the other one based on how many asteroids are included. Therefore in this thesis, the ring's radius is set for a fixed value of 2.8 AU and only the mass of the ring is adjusted that as a function of the number of asteroids that are to be individually included. The mass of the ring is directly and linearly proportional to the amplitude of the perturbation that it induces on the planet orbits (i.e Earth-Mars distance). Based on values that are provided by (Kuchynka et al., 2010), when including 50 of the most optimum asteroids individually, the amplitude of the perturbation will be at $472m$ which corresponds to a ring mass of $2.1879 \times 10^{20} kg$. Using the left Figure 2.5

one can extrapolate the mass for every possible N up to N = 500 using a simple linear relation $M_{ring} = C \times Amp_{perturbation}$ with constant C being equal to $C = 4.6353 \times 10^{17}$. Assuming the inclusion of only 11 optimum asteroids, the optimum mass of the ring will become $4.6353 \times 10^{20} kg$. After selecting the ring's properties, its perturbation on all planets needs to be included in the acceleration models. The mathematical formulation of a force acting on planets due to the presence of a ring as well as its validation are shown in Section 2.7.

To summarize, the complete solar system asteroid belt is modeled as 11 individually propagated asteroids shown in Table 2.2 that are optimally selected using MIQP analysis complimented with a ring that has a mass of $4.6353 \times 10^{20} kg$ with a radius of $2.8 AU$ centered at the solar system barycenter. Theoretically, this combination is capable of covering approximately 95 % percent of the total perturbation of the complete asteroid belt in the solar system judging by Figure 2.3 produced by (Kuchynka et al., 2010). This means, the virtual reality model developed in this thesis is capable of accurately, yet within the computational limitations, model the asteroid belt of the solar system making the scientific return of this thesis more valuable.

2.4 Simulation and observations time schedule

As the scenario that is to be tested in this thesis is most likely to happen in the near future, it is desirable to select a time frame in a the future which this scenario is expected to happen. There is also the capability of testing the hypothesis of what would have happened if laser ranging was implemented in the past but that would not be a very desirable or useful result as it is best to look on how much improvement one can make in the future.

The simulation time frame for this thesis is selected to be from 2020 to 2050. The reasoning for the start date is because of a number of important space missions are planned to become operational around that date, as shown in Table 2.3, making it an interesting and realistic choice of starting date for the simulation. The selected duration for estimation is very much tied to the computational budget that is available for this thesis and some preliminary tests have shown that performing more than 30 years of simulation is not computationally feasible with the asteroid combination shown in Section 2.3. However, long computational time spans are required to fully or at least mostly reconstruct the orbits of the planets. Uranus and Neptune have orbital periods beyond 100 years (i.e 111 and 170 years respectively) which means 30 years covers nearly one-fifth of their orbits. Ideally, one would require the estimation to cover at least one full orbit with observations covering the whole orbit as well to have a properly constrained orbit determination problem however in reality that is not the case. For instance, Neptune's observation history does not completely cover one full orbit of Neptune, which

result in its uncertainty becomes very large compare to other well constrained orbits (Folkner et al., 2014). Before that though, in the following subsection, some of the most significant future interplanetary missions are presented which is used to justify why the aforementioned time frame is a good time frame to choose to conduct this experiment.

2.4.1 Selected missions & Candidate planets for laser ranging

The confirmed missions are provided in 2.3.

TABLE 2.3: List of upcoming interplanetary missions that can be used for interplanetary tracking

Parent Planet	*Mission name*	*Operational time span*
Mercury	BepiColombo	2025-2027(28)
Venus	Venera-D	2026-2029
Mars	Mars 2020	2020-2022(25)
	ExoMars 2020	2020-2021
	Mangalyaan 2	2022-2023(25)
Jupiter	JUICE	2030-2034

Any of the missions that are shown in Table 2.3 can potentially be target of testing the laser ranging concept. In this thesis, for sake of simplicity, the observations are done to surface of the target planets rather than an orbiter around it. The reason for this decision is that it eliminates the requirement of defining each specific's mission orbit geometry as well as estimating orbiter's orbital parameters. In state of the art ephemerides generation processes, first the orbit of the orbiter around the target planet is determined accurately, then using the observation from the ground stations on Earth to the orbiter, the planetary ephemerides are determined. Having this process in this thesis adds a lot of complexity to the whole simulation and does not make any contribution towards answering the thesis question as the research question requires a laser ranging link to be available to a target planet, regardless of how this link is established.

When only laser ranging to surface of a planet is considered, then Mars becomes the only realistic candidate for having a laser link end. Venus has very dense atmosphere for laser ranging to be feasible due to susceptibility of visible light to refraction in different mediums. But that is not the driving factor of why Mars has been selected as the candidate planet to simulate laser ranging observations for. As also discussed by (Turyshev et al., 2004), In terms of scientific outcome, Mars is also one of the most interesting targets for testing laser ranging as its orbit is the most significantly effected by the asteroid belt. The masses of the many bodies in the asteroid belt are not so

accurately determined due to limited direct observations of them. This has made range measurements to Mars one of the significant contributing factor in improvement of the knowledge of asteroid masses. Hence accurate laser ranging to Mars can possible estimate these masses to potentially better accuracy which in return improves the orbit of Mars as well as other planets. The period of laser ranging to Mars is selected to be 3 years which is long enough to observe some the effect on asteroid masses while it is not too long. This duration is also inline with missions duration to Mars that are given in Table 2.3.

2.4.2 Observation Schedule

In this Section, the observation type and schedule used for each planet as well as the conditions that are used to ensure the simulated observations are physically feasible are explained. In order to determine a realistic observation schedule of each mission as well as selecting a realistic noise budget for each of them, a number of points are to be considered which are explained as follows. These points are derived based on analyzing literature and used as the main guideline to form assumptions regarding observation schedules selected in this thesis.

- Astrometric observation to gas giants, be it a transit observation of their Moons or a direct observation of the planet itself, are all assumed to be direct angular observation of that planet for sake of simplicity in simulating them in the observation model.
- It is assumed that ground stations (e.g Flagstaff) continue the current trend of direct angular observation to gas giants during the estimation period used in this thesis (i.e 2020 to 2050). This trend is shown in Figures provided by (Folkner et al., 2014) which shows how frequently observations to different planets are taken as well as the INPOP's observation database [3]. These trends are used as the main guideline for selecting the angular observation frequencies and the observation ucertainty budget for Jupiter, Saturn, Uranus and Neptune that are shown in Table 2.4.
- It is assumed that ground stations (e.g Arecibo) seize to conduct any direct radar ranging to inner planets during the estimation period used in this thesis (i.e 2020 to 2050). Hence, the missions to inner planets provided in Table 2.3 are the only source of range observations to these planets. The reason for this assumption is because these radar stations have not been conducting any radar range observations in more than a decade or so as can be seen by actual observation schedules shown in(Viswanathan et al., 2017), (Folkner et al., 2014) and INPOP's observation database.

[3] http://www.geoazur.fr/astrogeo/?href=observations/base

- It is assumed the observations that are made to the the missions that are given in Table 2.3 are mainly direct range observations (i.e radio range) and there are no angular observations made to these missions (e.g VLBI). The reason for this is directly derived from observation schedule of actual past missions shown in (Viswanathan et al., 2017) and (Folkner et al., 2014). As an example, there have been 25,000 range observations to Venus Express from 2007 to 2012. In the same time interval, only 46 VLBI observations have been made of this mission which are done very inconsistently with accuracy that is less than the accuracy of range observations. Hence the range observations to Venus Express trumps the VLBI observations as they are done during the same time interval and range observations having higher accuracy. This is also true for other planets which show mainly range observations to their orbiters or landers. It is indeed true that VLBI observations has been very beneficial in determining planetary ephemerides, for instance, as also shown in Table 3.1, VLBI observation of Magellan from 1990 to 1995 has been the only source of accurate observation to Venus during that time period which allowed for accurate determination of Venus ephemerides during that time period. This is because there were no better observations available during that time period so including them is beneficial and essential. Hence for simplicity in this thesis, only consistent range observations done to missions shown in Table 2.3 are used as the main mean to determine the orbit of their respective planet.

- Observation schedule of missions provided in Table 2.3 are selected based on schedule of similar interplanetary missions used in past. Same is true for their induced noise profile which is selected based on combination of noise budget of the past missions. Studies shown for BepiClombo mission indicate that it can achieve range observation accuracy of at least few meters but optimistically, these uncertainty can be reduced to less than a meter by doing the observation in a 5-way link configuration while exploiting various reduction techniques explained in (Tommei et al., 2010). In this thesis observations to BepiClombo are assumed to be a direct range observations to this mission hence it assumes a conservative uncertainty budget of a few meters rather than the optimistic sub meter level one. To compare this uncertainty budget to past missions to Mercury, one can look at MESSENGER mission which managed to achieve range observation uncertainty of around 10 meters (Viswanathan et al., 2017) which shows range observation accuracy of a few meters is indeed realistic.

  Venera-D range observation accuracy is directly taken from Venus Express range observation accuracy as there are not yet conclusive studies on uncertainty budget of this mission and the missions have similar characteristics(Zasova et al., 2017), Venus Express achieved range uncertainty of about 10 meters which is also the value chosen for Venera-D mission. Similar justification is used for future Mars missions as studies shown that they are expected to continue the current trend

range observation accuracy to Mars (Kuchynka and Folkner, 2013). Mars Odyssey and Mars Express both achieved range observation uncertainty of about 5 meters folkner2014planetary which is also what is selected for the future Mars missions. For JUICE, the observation uncertainty is selected based on missions characteristics presented in (Plaut et al., 2014).

- All the different missions to Mars that are shown in Table 2.3 are summarized into one mission or linkend from 2020 to 2025 for simplicity of observation scheduling and systematic noise implementation.

Based on the above assumptions, the observation schedule to each individual planet can be determined. A summary of the observations to all the planets and different missions are provided in Table 2.4 which is mainly gathered from (Viswanathan et al., 2017) and schedules shown in (Folkner et al., 2014).

TABLE 2.4: Observation scheduling of each link for each planet. Each line represent one link

Observation Scheduling				
Planet	*Duration*	*Frequency*	*Type*	*σ of the noise*
Mercury	2025 to 2028	6 Obs per hour repeated every day	BepiClombo radio range	±3 m
Venus	2026 to 2029	6 Obs per hour repeated every day	Venera-D radio range	±10 m
Mars	2020 to 2025	6 Obs per hour repeated every day	Combined Mars mission radio range	±5 m
	2020 to 2023	6 Obs per hour repeated every day	Hypothetical laser ranging phase	±5 mm
Jupiter	2030 to 2034	6 Obs per hour repeated every day	JUICE radio range	±100 m
	2020 to 2050	180 obs per 90 days repeated every 90 days	Direct astrometric	±200 mas
Saturn	2020 to 2050	180 obs per 90 days repeated every 90 days	Direct astrometric	±200 mas
Uranus	2020 to 2050	180 obs per 90 days repeated every 90 days	Direct astrometric	±200 mas
Neptune	2020 to 2050	180 obs per 90 days repeated every 90 days	Direct astrometric	±200 mas

2.4.3 Observation viability conditions

The simulated observations are based on solving light time equation shown in Section 2.5 which is completely theoretical and do not consider whether the ground station is physically capable of making the observation. Hence, to ensure the simulated observation are physically possible, are a number of conditions are applied that checks whether the simulated observation is feasible or not. If any of the conditions provided below are not satisfied when solving the light time equation, then that observation is removed from the list of feasible observations.

- **Planet's elevation angle with respect to the ground station:** For ground station to be able to observe the planet, it needs to be in line of sight of the station. The target planet's center of mass is selected a minimum of 2.5 degrees elevation angle with respect to the ground station to ensure the planet is in line of sight of the ground station.

- **Moon osculation:** Even though this can be a rare occurrence, the Moon is set not to break the line of sight of target planet and the ground station.
- **Sun avoidance angle:** The Sun is set not to block the ground stations from making the observations to target planets. On one hand, the observation noise scales up the closer the station is pointed towards the Sun due to solar flux but on the hand, to capture the relativistic effects, its best to have observation as close to Sun as possible as the effect of Sun's gravity on electromagnetic wave becomes larger the closer it is passing from it. This allows for getting better constraints for PPN parameter γ when utilizing laser ranging (see Section 2.9.3). In this thesis, the Sun avoidance angle is selected to be larger than 1 degree for laser and radio ranging observations to capture this effect as good as possible.

2.5 Observation models

In this Section, the models that are used to simulated range and angular observations are presented. In order to simulate the observation between the two bodies, first the light time between the two bodies are determined. Equation 2.1 shows how the light time, t_{LT}, between two bodies are computed. In this Equation, with Δt^1 refers to the first order relativistic time correction due gravitational potential of the involved bodies (i.e the $\frac{1}{c^2}$ term presented in full light time equation provided by (Moyer, 2005) and r_r and r_t are the positions of the receiving and the transmitting ends of the link. Since transmitter and receiver are moving relative to one another and speed of light is not infinite, the true light time is approximated iteratively. This is done by dividing the distance between receiving and the transmitting ends at $t = t_t$ by the speed of light. Then using the calculated light time, the displacement that both transmitter and receiver go through during that time is computed and from the newly computed positions, a new light time is then computed. This process is repeated until the change in light time at each iteration becomes negligibly small.

$$t_{LT} = t_r - t_t = \frac{|\bar{r}_r - \bar{r}_t|}{c} + \Delta t^1 \tag{2.1}$$

After computing the light time between the two desired bodies (i.e transmitting and receiving ends) then that information can be used in order to simulate the desired observation from the position function of those bodies. In the following subsections, the observation models for simulating one-way range, two-way range and angular position are provided. The below Equation is as a function of the transmission time.

2.5.1 One-way range simulation model

The one-way range is simulated using Equation 2.2. In this Equation, t_1 is the time where the signal is transmitted from the transmitter and the time at reception is $t_1 + t_(LT)$ with $t_(LT)$ being light time value that is computed used Equation 2.1.

$$h^{(1)}_{t_t=t_1} = |\bar{r}_r(t_1 + t_{LT}) - \bar{r}_t(t_1)| \tag{2.2}$$

2.5.2 Two-way range simulation model

For two-way range, which is the configuration used for laser ranging in this thesis, Equation 2.3 is used which is just the summation of two one-way ranging configuration. Equation 2.3 assumes that there is no delay between the reception and re-transmission time and re-transmission is done instantaneously. Equation 2.3 also does not include the additional Δt term in case the laser ranging is done asynchronously as in this thesis, echo ranging is assumed (i.e signal is re-transmitter back to the ground station as soon as it is received by the receiver), In Equation 2.3, t_1 is the time where the transmitter first transmit the signal towards the receiver and t_2 is the time when the receiver receivers and re-transmits the signal back to the ground station. The below Equation is as a function of the transmission time.

$$h^{(2)}_{t_t=t_1} = |\bar{r}_r(t_1 + t_{LT1}) - \bar{r}_t(t_1)| + |\bar{r}_t(t_2 + t_{LT2}) - \bar{r}_r(t_2)| \tag{2.3}$$

2.5.3 Angular position simulation model

The angular observations are declination, $h^{(\delta)}$, and right ascension, $h^{(\Omega)}$, of the planets relative to the ground stations. These observations are computed using Equation 2.4 in which x and z denote the Cartesian components of the position vector of the receiver or transmitter at times tamps shown in the equation.

$$\begin{aligned} \mathrm{h}^{(\delta)}_{t_t=t_1} &= sin^{-1}\left(\frac{z_r(t_1 + t_{LT}) - z_t(t_1)}{|\bar{r}_r(t_1 + t_{LT}) - \bar{r}_t(t_1)|}\right) \\ \mathrm{h}^{(\Omega)}_{t_t=t_1} &= cos^{-1}\left(\frac{x_r(t_1 + t_{LT}) - x_t(t_1)}{|\bar{r}_r(t_1 + t_{LT}) - \bar{r}_t(t_1)|cos(\delta)}\right) \end{aligned} \tag{2.4}$$

2.6 Observation noise treatment

The observations that are simulated in this thesis are based on solving the state equation between the two bodies. So a realistic noise profile needs to be put on the observations to reenact the limitations that are available in the actual observations. The noise profiles are divided into stochastic and systematic noise which come from different sources in

the observation environment. Systematic noise represent the noise that is typically time dependent and it also includes the environmental sources that leave a certain specific signature on the observations. For instance atmospheric interference, solar activity or even presence of unmodeled forces which leave their signature on the observations, either as short period or long period variations. Stochastic noise consist of random walk that is present in the recorded observations which come from sources that were explained in Section 1.2.

The total noise that is applied on the observation is the summation of stochastic and systematic noise depending on the observable type that is used which is shown in Equation 2.5 with h being a realization of an observation

$$h_{real} = h_{ideal} + \delta h_{sys} + \delta h_{stoch} \tag{2.5}$$

The stochastic component of the noise is simply realized by sampling a normal distribution function with a user-defined standard deviation. The systematic component however, slightly more complex to implement correctly. Section 2.6.1 explains how the systematic noise is defined in this thesis. In case when the Virtual Reality and the estimation model are dynamically identical, the dominating factor on the residuals become the noise profile that is applied on the observation. In Section 3.3 the induced noise profile on the observations as well as the effect that it has the post-fit residuals and converged solution of the problem are shown. This gives an insight on how sensitive are the estimated orbits to the profile of the noise as well as give some ideas on the reliability of the noise function purposed in this Section.

2.6.1 Systematic noise function

Modeling systematic noises correctly is generally very challenging as it requires one to exactly know the noise sources, their mathematical formulation or a general idea of how they behave and finally, how different sources interact with each other when added together or superimposed.

In this thesis a number of linkends and missions are created each having their unique characteristics depending on the target planet and the missions type. Hence the systematic noise of the observations for each linkend and mission is typically unique to that mission and is defined based on the mission characteristics. Designing individual systematic noise profile for each of these linkends based on their specific mission characteristics is not only technically challenging to achieve but also very tedious to do. Also it will drastically the flexibility of the developed simulation model as it will only become capable of analyzing one specific case or mission. One the achievements of this thesis is to have a sandbox and an open framework to test any possible hypothesis in the future without having to redesign the whole model from scratch and by only adjusting very

simple input parameters.

To maintain flexibility of the developed simulation model and at the same time eliminate the tedious process of designing a unique noise profile from scratch for every single linkend of mission that is added to the simulation, the best approach would be to generalize the systematic noise generation process. This is done in a way that a realistic systematic noise can be generated for each mission by simply adjusting a number of input parameters to tamper with the behaviour of the noise profile for each specific mission. This process make noise generation in this simulation a global approach but yet specific enough to be applicable to independent missions.

There are theoretical methods for generating time dependent noise such as the one purposed by (Timmer and Koenig, 1995) in which spectral theory is utilized to generate a non deterministic time series which illustrates a $(\frac{1}{f})^{\beta}$ spectrum (Timmer and Koenig, 1995). Inspired by the aforementioned method, a simplistic approach is purposed in this thesis which at its core follows a similar procedure as the one given in (Timmer and Koenig, 1995) yet it is slightly more simplified to apply in this thesis. More specifically, the newly purposed process eliminates the need to generate the noise in frequency domain and subsequently the requirement of transformation and representation of noise in the time domain as all the operations are directly performed in the time domain. This process is explained in the following paragraph. Th downside of this method is that it requires a number of trial and errors with various settings in order to generate a noise profile that seems realistic. Another downside is that this noise profile is generated theoretically therefore it will never be based on actual events that happen in reality hence it becomes very complex to actually know whether this theoretically modeled noise covers the superposition of full spectrum of noise sources that exists in reality.

The idea behind the systematic noise generation function is to superimpose a number of randomly defined trigonometric functions (i.e sine or cosine) that their amplitude, phase and frequency are selected randomly from a pre-defined domain bounded by a set of user defined values. The boundaries of amplitude and frequency domain are carefully selected such that the noise profile capture the signature of both short and long noise variations that exists in reality while the magnitude of the noise remain within the required bounds which are given as σ in Table 2.4. In this process, each individual missions has its own set of amplitude or frequency domain which allows the noise profile to be unique to each linkend.

To make sure the systematic noise profile remain realistic, the timespan of each mission is divided into a number of arcs and a unique noise profile is added to the observations per arc. This eliminates the issues of having one single behaviour dominating the whole noise profile which is inline with reality. For instance, in reality it can be observed that a certain noise signature might only be present during a certain timespan. To avoid

having discontinuity in the noise profile, the noise values are set to accumulate over time, meaning that the information from the previous arcs are carried over to the next arc resulting in a continues and realistic behaviour of noise. The term realistic here does not necessarily mean the generated noise profile directly and accurately represent what is happening in reality. The idea is that it merely tells the estimation model that there exists a certain non deterministic time dependent behaviour in the simulated observations which its shape is similar to what have been observed in the uncertainty budgets of actual observations. This results in the estimation to be performed in an environment that is closer to what happens in reality. This is believed to be more realistic than performing a simulation with only having Gaussian noise or even no noise at all as those approaches typically result in overly optimistic errors. The mathematical formulation of the generated noise function is given in Equation 2.6

$$\delta h^{sys}_{(t,i)} = \sum_{i=1}^{i} \sum_{n=1}^{n} A_{(i,n)} sin(2\pi f_{(i,n)} t + \phi_{(i,n)}) \tag{2.6}$$

In Equation 2.6, $\delta h^{sys}_{(t,i)}$ represent the systematic noise at time t of the i^{th} arc, i represents the number of arcs the observation timespan is divided to and n represents the number of trigonometric functions that are added together. Only sine function is selected as cosine is just a phase shifted sine which makes no difference for this process. Values $A_{(i,n)}$, $f_{(i,n)}$ and $\phi_{(i,n)}$ represent the amplitude, frequency and phase of the sine function at i^{th} arc of n^{th} function.

To ensure the input frequency domain represent the actual output noise frequency which is un-tampered by time, the time vector per arc is normalized between 0 and 1, ensuring the noise behaves according to the given frequency domain independent of the value of time. The parameters in the systematic noise function are selected using trial and error and fine tuning until the noise profile looks desirable. The frequency values are selected from a domain of between -10 and +10 which resulted in producing noise profiles that cover short and long period variations with overall. The amplitude domain is between $-\sigma$ and $+\sigma$ of the observation uncertainty of each mission and the phase domain selected between -2π and 2π for each arc. Section 3.3 explains on which observations the systematic noise profile are applied to, shows the applied noise profile themselves, the effect they have on the the estimation results (i.e verification) are provided in Section 3.3. After fine tuning. a list of settings that are selected to produce the noise profile with are shown in Table 2.5.

TABLE 2.5: List of settings used for systematic noise profile (for Equation 2.6)

Number of arcs - i	10
Number of superimposed functions - n	10
Phase domain - ϕ	[-2π, 2π]
Frequency domain - f	[-10,10]
Amplitude domain - A	[-σ,σ] (Table 2.4)

2.7 Acceleration settings

The acceleration model that is used in both Virtual Reality and estimation model follow from an extended point mass Newton's acceleration. The full equations of motion is shown in Equation 2.7 which shows all the different acceleration models that are used to describe the motion of the bodies in solar system.

$$\ddot{\bar{r}}_i = \ddot{\bar{r}}_{i,pm} + \ddot{\bar{r}}_{i,SunJ2} + \ddot{\bar{r}}_{i,Schwarz} + \ddot{\bar{r}}_{i,Lens} + \ddot{\bar{r}}_{i,ring} \tag{2.7}$$

In Equation 2.7, $\ddot{\bar{r}}_i$ is the total acceleration that i^{th} body undergoes which is the combination of all the acceleration models that the body is affected by. Each of the individual component of the equations of motion and their mathematical term are given in Equations 2.9 to 2.12. The accelerations are computed in a barycenteric ecliptic coordinate system (i.e ECLIPJ2000 as defined by Navigation and Ancillary Information Facility [4]) which its xy-plane lies in the ecliptic plane with its x-axis pointing towards vernal equinox which is at the intersection of mean ecliptic plane with mean equator of epoch J2000 [5].

1. **Point mass acceleration:** The first component is $\ddot{\bar{r}}_{i,pm}$ which is the point mass acceleration between all the bodies mentioned in Section 2.2 (i.e Sun, Mercury, Venus, Earth, Moon, Mars, Jupiter, Saturn, Uranus and Neptune) as well as the individually propagated asteroids shown in Table 2.2. In Equation 2.8, i and j are the bodies undergoing and exerting the acceleration with M_j being the mass of the exerting body. $\bar{r}_{i,j}$ is the vector position vector between body i and j.

$$\ddot{\bar{r}}_{i,pm} = \sum_{i \neq j} \frac{GM_j}{r_{ij}^3} \bar{r}_{i,j} \tag{2.8}$$

[4] https://naif.jpl.nasa.gov/pub/naif/toolkit_docs/C/req/frames.html
[5] 27th International Astronomical Union General Assembly, Resolution B3, 2009

2. **Sun's oblateness effect:** Equation 2.9 (Standish and Williams) is computed in Sun's body reference fixed frame with J_2 being the Sun's oblateness coefficient and $P(f)$ being the Legendre polynomial function of degree n. Angle ϕ represent the planet's latitude with respect to the Sun's body fixed frame. This acceleration is added to the point mass acceleration show in Equation 2.8 after its transformed into a barycenteric ecliptic reference frame that was mentioned earlier in this sectio. Details on how this transformation is done can be found in Chapter 5 of (Petit and Luzum, 2010).

$$\ddot{\bar{r}}_{i,SunJ2} = -\frac{GM_{Sun}}{r^2}\left(J_2\frac{R_s^2}{r^2}\begin{bmatrix} 2P_2(sin\phi) \\ 0 \\ -cos\phi P_2'(sin\phi)\end{bmatrix}\right) \tag{2.9}$$

$$P_n(f) = \frac{1}{(-2)^n n!}\frac{d^n}{df^n}(1-f^2)^n$$

3. **Sun's Schawrzchild relativistic correction:** This relativistic term has the largest effect on the planetary ephemerides compared to the other two and provides a relationship between the two PPN parameters β and γ, allowing the estimation of either of this parameters during the estimation process. This effect is only accounted between Sun and other bodies and not between every bodies in the solar system. The reason for this is the magnitude of this effect is the largest for the Sun only and it becomes extremely small between other bodies which can be seen by looking at Equation 2.10. (Petit and Luzum, 2010)

$$\ddot{\bar{r}}_{i,Schwarz} = \frac{GM_{Sun}}{c^2 r_i^3}\left(\left[2(\beta+\gamma)\frac{GM_{Sun}}{r_i} - \gamma\dot{\bar{r}}_i\cdot\dot{\bar{r}}_i\right]\bar{r}_i + 2(1+\gamma)(\bar{r}_i\cdot\dot{\bar{r}}_i)\dot{\bar{r}}_i\right) \tag{2.10}$$

This acceleration scales with mass of the exerting body as well as inverse of the speed of light squared which makes the Sun the most dominant body to consider.

4. **Sun's Lens-Thirring effect:** This is another important relativistic effect to consider which has the second most significant relativistic effect. This effect takes into account the secular precessions of the argument of pericenter of the planets that are orbiting an spinning body (i.e Sun). Therefore, it is a function of the angular momentum of the body it is orbiting. Equation 2.11 provides the mathematical expression of this effect (Petit and Luzum, 2010) with parameter $\bar{I}$ being the angular momentum vector of the Sun. Sun's angular momentum is assumed to only have a component in polar direction and the other component are assumed to be negligibly small (i.e $I_{zz} = 190 \times 10^{39}[\frac{kgm^2}{s}]$ which I_{xx} and I_{yy} assumed to be zero with z representing the polar direction).

$$\ddot{\bar{r}}_{i,Lens} = (1+\gamma)\frac{GM_{Sun}}{c^2 r_i^3}\left(\frac{3}{r^2}(\bar{r}_i\times\dot{\bar{r}}_i)(\bar{r}_i\cdot\bar{I}) + (\dot{\bar{r}}_i\times\bar{I})\right) \tag{2.11}$$

5. **Ring's acceleration:** The ring acceleration model is provided in Equation 2.12 extracted from (Kuchynka et al., 2010) which shows the acceleration due to a thin ring with homogeneous mass on a point mass any where in space.

$$\ddot{\bar{r}}_{i,ring} = -\frac{2GM_{ring}}{\pi\alpha(1-\beta)\Gamma^{\frac{3}{2}}}\left[\alpha E(\beta)\bar{r}_p + ((1-\alpha)K(\beta) - E(\beta))r_{ring}\bar{i}\right] \tag{2.12}$$

With parameters α, β and Γ defined in Equation 2.13

$$\begin{aligned} \alpha &= \frac{2r_p r_{ring} cos(I)}{r_p^2 + r_{ring}^2} \\ \beta &= \frac{2\alpha}{1+\alpha} \\ \Gamma &= r_p^2 + r_{ring}^2 + 2r_{ring}r_p cos(I) \end{aligned} \tag{2.13}$$

In Equations 2.12 and 2.13, r_p is the position vector of the point mass subject to the acceleration, r_{ring} is the radius of the ring. Angle I is the angle between the vector from the center of the ring to the a point mass p (i.e $\bar{r}_p$) and its projection on the ring's plane. Vector $\bar{i}$ is the unit vector in the direction of the projected vector $\bar{r}_p$ on the ring's plane. Finally, Functions $E(\beta)$ and $K(\beta)$ represents the first and second order elliptical integral provided in Appendix A. The ring's plane coincides with the plane of ecliptic with its origni at the barycenter of the solar system while its characteristics were already provided in Section 2.3.2. It is also required to compute the partial derivative of this acceleration model with respect to the estimated parameters for the estimation but computing the derivatives of Equation 2.12 analytically is extremely tedious. Hence the partials for this function are computed numerically using the method described in Appendix B. This acceleration model was not part of TUDAT's library of verified acceleration models and is implemented in TUDAT by the author himself. Hence its implementation in TUDAT needs to be validated to ensure its accelerations are computed correctly. This is validation done in Section 3.2.

2.8 Integration settings

The selected integration setting for this simulation is a fixed step size Runge-Kutta-Fehlberg 78 (Cartwright and Piro, 1992) which is a 7^{th} order integrator. The selected integrator and its time steps are important to ensure that the estimation results are not dominated by integration error. To test which time step is sufficiently small enough such that it does not dominate the true error of the estimation, yet it manages to perform the simulation within the computational limits of this thesis, a number of tests have been performed. In this test setup, a 30 year estimation is performed which includes all the major bodies mentioned in Section 2.2. In this simulation, only the state vector of Mercury is estimated using ideal (i.e no noise) and consistent observations to Mercury

over the whole simulation period. This simulation is run for a number of different time steps, namely 60, 30, 20 and 5 minutes and the estimation results are compared to one another. Since no noise is present in the observations and the truth and estimation model are identical, the estimated ephemerides of Mercury will only become limited to the integration error and numerical precision of the estimation. Conducting this test allows one to see how large the integration error will on the estimated ephemerides will be and whether it is the dominating factor in the estimation.

It was found that for all cases, the formal error of the estimation remains the same as the observation weights for all cases are the same. But when the estimated results are compared to true values from the truth model, then one can observe the effect of integration error as that is the only source that causes the difference between the results. The formal error of the Mercury's estimated initial position for all were found to be at less than cm level. The true error of the estimated initial position were also at sub cm level for all cases expect for the time steps of 60 and 30 minutes which had true error of 3 to 4 cm which are larger than the formal error. An integration time step of 20 minutes was found to be a good enough choice as it is not either too small that it would take too much memory to perform the estimation, yet it is small enough that it is small enough to produce sub cm level estimation results that do not exceed the formal error (i.e do not dominate the estimation error). It is later proven in Section 4.1, specifically as is shown in Figure 4.8, that this selection is indeed a valid choice as the errors in estimated orbit when laser ranging is applied are at a few centimeter level and integration error of less than cm level is sufficient.

2.9 Parameters for estimation

This section attempts to justify what parameters are and are not estimated as well as the assumption that goes with estimating each parameter. Justification for estimating planetary state vector, dynamical and relativistic parameters and asteroid mass parameters are explained individually.

2.9.1 Estimating planetary state vector

The selected planets that their initial position and velocity vector are set to be estimated are Mercury, Venus, Mars, Jupiter, Saturn, Uranus and Neptune. The states of the Earth and Moon are not estimated during the estimation process because the estimation problem becomes ill-conditioned. All the observations to the planets are simulated with respect to the Earth which means their positions in space are constrained in an absolute sense. This however is not the case for Earth itself as there are no constraints on its position (i.e no absolute observations of the Earth itself are used) and since all

observations are done relative to the Earth, having Earth as a free parameter will result in problem to be badly conditioned. Performing a singular value decomposition of the information matrix for the case when Earth's state were included as an estimable parameter displayed much higher singularity compared to a case where Earth's state were not included (i.e the condition number of the estimation increased by a factor of 10^4 to a value of 10^{16}).

Not estimating the Earth and Moon's state vector is equivalent of putting a very accurate apriori uncertainty on their position meaning their position is pretty much determined by their apriori knowledge. This essentially means that the results that are produced in this thesis are based on the assumption that the uncertainty in orbit of the Earth (and Moon) remains unchanged with introduction of interplanetary laser ranging to Mars. In other words, interplanetary laser ranging to Mars does not significantly improve the current knowledge of Earth and Moon's orbit.
This assumption is not ideal but it can be partially justified by the fact that the Earth-Moon barycenter is currently known to an accuracy of about a few meters and is mainly determined by the laser ranging that has bee done to the Moon. So getting a significant improvement in Earth's position with introduction of laser ranging to a point where its cascade effect significantly improves the orbit of other planets is far fetched. This does not mean that there will be no effect as one part of the solar system's dynamical coupling is being eliminated from the estimation but since including the Earth causes ill-conditioned and a diverging problem, fixing the Earth and Moon orbit becomes the only alternative option.

Neglecting Earth from estimation does not mean that the rest of the results provided in this thesis will become invalid or invaluable. The effect of laser ranging on orbit of Mars itself and other planets' ephemerides, mass parameter of the estimated asteroids and dynamical parameters can still be investigated. It is expected that inclusion of the Earth in the estimation will actually make results even better compared to when its not included since there an additional component is solar system ephemerides that will be prone to improvements. It will also result in a better correlation between the planets orbital parameters as no dynamical coupling is neglected. Another way to look at it is that not estimating the Earth's state vector means that the effect of laser ranging on planetary ephemerides is not explored to its full potential.

2.9.2 Estimating asteroid mass parameter

Other than estimating the planetary state vector, the mass parameter of some of the bodies in the asteroid belt are also estimated (i.e the ones shown in Table 2.2). The effect of estimating asteroid masses alongside ephemerides is two-folded. One is that one can directly see the effect of having more accurate ephemerides on getting a better

knowledge of the asteroid belt which in turn results in further improvement in planetary ephemerides. An extensive discussion was given in Section 2.3 which explained which asteroids are selected for estimation and why. To summarize, the mass parameter of the 11 of the most optimally selected asteroid are estimated during the estimation period. These asteroids are shown in Table 2.2.

2.9.3 Estimating relativistic PPN parameter & Sun's J_2

Relativistic parameters γ and β are both important to be estimated in order to measure the extend of laser ranging effect on estimating relativistic accelerations. But naturally there is a very high correlation between the Sun's J_2 effect and the PPN parameters γ and β as it is quite complex to distinguish the effect of on these parameters. As was mentioned in Section 2.4.3, a small Sun avoidance angle of 1 degree is selected to better distinguish Sun's J_2 effect from relativistic acceleration to ultimately de-correlate Sun's J_2 parameter from γ and β. However this does not entirely eliminate the high correlation between PPN parameters themselves as these relativistic effects leave similar signatures on planetary ephemerides as is explained in (Genova et al., 2018) (i.e their effect are mainly seen in planetary orbits' precession of their perihelion)

It is common practice in state of the art ephemerides generation processes to fix the values of γ and β to their nominal values and perform the estimation which is the case in JPL's latest ephemerides (Folkner et al., 2014). The argument behind not estimating PPN parameters in state of the art ephemerides is that their focus is to simply produce the most accurate ephemerides based on the currently available best estimate of PPN parameters and not so much about performing relativistic studies. Typically, the PPN parameters are estimated in an exclusive study which is performed under much more constrained estimation environment, typically using data for a specific mission like it is done in (Genova et al., 2018), (Verma et al., 2014) or (Shapiro et al., 2003). In the studies where the main goal is to conduct relativistic tests and improve PPN parameters uncertainty budget, specialized techniques are used during the estimation to constraint PPN parameters γ and β by making using of constraint equations that provide a solution in form of a direct relationship between these parameters. One of these constraint equation is the Nordtvedt parameter which provides a solution in form of a direct relationship between γ and β allowing proper decorrelation and estimation of PPN parameters (Genova et al., 2018).

As was mentioned in Section 1.2, the focus of this thesis is to mainly produce ephemerides using interplanetary laser ranging and observe the dynamical coupling between the planetary states. Therefore, performing an extensive relativistic experiments and testing general relativity is not directly part of the goal of this thesis, so it becomes very much valid to simply follow the same procedure that is used in (Folkner et al., 2014) and fix

the PPN parameters to their nominal values and perform the estimation that way. In other words, completely ignoring the effect of laser ranging on relativistic parameters. However, the model that is setup in this thesis has the capability of estimating PPN parameters which can give some preliminary insights on the potential effect of laser ranging on relativistic parameters as well as their corresponding effect on the planetary ephemerides, improving overall science return of this thesis. Also estimating PPN parameters can be used as a verification that the way the models that are setup in this thesis are working properly and it has the capability to estimate PPN parameters with the same level of uncertainty as it can be currently achieved in literature which is showcased in Section 4.3 and Table 4.2.

The simplest way of estimating the PPN parameters in this thesis while avoiding having to deal with high correlations between them is to only estimate one of the parameters, γ. This eliminates the need of using constraint equations which introduce some complexity to implement properly. However, this means a crucial assumption is being made. With only estimating γ one essentially assumes that the Nordtvedt parameter is equal to its nominal value, resulting in all relativistic effects to be combined and represented by γ only. Although estimating γ only does not give the full picture of the effect of laser ranging on all relativistic parameters, it provides on good insight on laser ranging potential. For example, if cascade effect of laser ranging results in an improvement in Mercury's orbit, then theoretically one should see an improvement in γ and Sun's J_2 uncertainty. By estimating γ with and without interplanetary laser ranging, one can easily check whether one achieves the expected level of improvement in γ's uncertainty which further solidify the results given in this thesis. Since it is assumed that Nordtvedt parameter is equal to its nominal value, any improvement that is seen in γ can also be attributed to β as well as they are directly related with Nordtvedt relation.

All in all, apart from the planetary states and asteroid masses, it is decide to estimate PPN parameter γ as well as the Sun's oblateness parameter (i.e J_2) to not only get an idea on relativistic gravitation but also on the effect of laser ranging on better determining Sun's shape.

2.9.4 Summary of estimated parameters

TABLE 2.6: List of all estimated parameters with their nominal values that are used to initialize the simulation

Parameter Number & Name	*Notation & Unit*	*Nominal value*
(1-6) Mercury's initial position & velocity	$r_{m,0}$ - $[m]$	[-8377752361.207219, -67982946561.26395, -4926303389.157013]
	$v_{m,0}$ - $[m/s]$	[38618.78541881038, -2991.641382662385, -3787.793486511041]
(6-12) Venus's initial position & velocity	$r_{v,0}$ - $[m]$	[107494157695.4842, 10475228222.92837, -6104078691.231328]
	$v_{v,0}$ - $[m/s]$	[-3176.888982638236, 34728.00359571239, 659.4694270184846]
(12-18) Mars's initial position & velocity	$r_{M,0}$ - $[m]$	[-197429968937.8544, -132172972866.3419, 2040636733.965869]
	$v_{M,0}$ - $[m/s]$	[14476.83041447877, -17993.3732409705, -732.1140174180481]
(18-24) Jupiter's initial position & velocity	$r_{J,0}$ - $[m]$	[78696927591.92229, -776865410111.0364, 1461343537.686944]
	$v_{J,0}$ - $[m/s]$	[38618.78541881038, 1939.618778997667, -295.249188338075
(24-30) Saturn's initial position & velocity	$r_{S,0}$ - $[m]$	[567854314153.4276, -1388209698714.721 ,1532088987.268128]
	$v_{S,0}$ - $[m/s]$	[8405.365727700491, 3629.005176386816, -397.7382621617414]
(30-36) Uranus's initial position & velocity	$r_{U,0}$ - $[m]$	[2426560356277.195, 2426560356277.195, -25109106295.94876]
	$v_{U,0}$ - $[m/s]$	[-3963.027571449441, 5256.19021502804, 70.8835883472557]
(36-42) Neptune's initial position & velocity	$r_{N,0}$ - $[m]$	[4374142156733.883, -951173880784.4816, -81218851477.3933]
	$v_{N,0}$ - $[m/s]$	[1118.874972727693, 5343.470123633252, -135.8023319747549]
(43) PPN parameter γ	γ	1.0
(44) Ceres mass parameter	μ_{ceres} - $[km^3/s^2]$	63.18
(45) Vesta mass parameter	μ_{vesta} - $[km^3/s^2]$	17.74
(46) Pallas mass parameter	μ_{pallas} - $[km^3/s^2]$	14.08
(47) Hygiea mass parameter	μ_{hygiea} - $[km^3/s^2]$	5.84
(48) Euphrosyne mass parameter	μ_{euph} - $[km^3/s^2]$	3.58
(49) Intermanta mass parameter	μ_{inter} - $[km^3/s^2]$	2.60
(50) Davida mass parameter	μ_{davida} - $[km^3/s^2]$	2.56
(51) Eunomia mass parameter	μ_{eunom} - $[km^3/s^2]$	2.11
(52) Juno mass parameter	μ_{juno} - $[km^3/s^2]$	1.99
(53) Europa mass parameter	μ_{europa} - $[km^3/s^2]$	1.75
(54) Doris mass parameter	μ_{doris} - $[km^3/s^2]$	1.73
(55) Sun's J_2 parameter	J_2	2.0 $\times 10^{-7}$

Chapter 3

Validation

This Chapter deals with validating the simulation that is setup in Chapter 2. It attempts to not only answer the questions raised below but also quantify the impact of the assumptions that were made while modeling the simulation. In particular, it validates the assumptions made regarding the parameters that are include and excluded in estimation (Section 2.9), selected observation scheduling (Section 2.4.2), the way the observation uncertainty and noise budget is treated (Section 2.6) etc. This Chapter starts with Section 3.1 which mainly answer the following questions and validates the overall simulation in terms of its general capabilities of producing planetary ephemerides.

- How the planetary orbit uncertainties produced in this validation compare to the state of the art planetary orbit uncertainty?
- Is the method introduced in Section 2.1 a valid approach for assessing the uncertainty of estimated parameters?
- Is using simulated observations with artificially introduced noise a valid approach?

The strategy for validating the above three points is to perform a simulation using a similar observation scheduling and simulation settings which were used to generate the results given in (Folkner, 2010) (i.e JPL's state of the art model) and asses how well the models developed in this thesis are capable of converging to the solutions provided by (Folkner, 2010). Section 3.1 briefly explains the overall settings used for validation and compare the generated results with the one provided in literature in order to validate the raised question.

Sections 3.2 and 3.3 in this Chapter are dedicated specifically in validating the implemented asteroid ring model introduced in Section 2.7 and the developed systematic noise generator introduced in Section 2.6.1. Section 3.3 performs a dedicated study to quantify the effect of the systematic noise that was put on certain observations. The

results of Section 3.3 are shown in an attempt to display how the systematic noise model that was designed in Section 2.6.1 contributes in having a more realistic estimation results and whether the method is robust and realistic as well as determining how sensitive the ephemerides are to the systematic noise.

3.1 Validation simulation setting & Results

To validate whether the model provided in this thesis is an accurate representation of reality, an estimation is performed by following a similar settings used by JPL's DE423 ephemerides generation process using the same and actual observation schedules which can be found in (Viswanathan et al., 2017) and (Folkner et al., 2014) and the output of the estimation is compared to the propagated formal uncertainties of DE423 presented in (Folkner, 2010). The reason why the comparison is done with respect to DE423 (i.e a version before the latest JPL's DE430 model) is simply because author had only access to the propagated uncertainty of all estimated planet positions for that particular version which was publicly released. In any case, the main difference between DE423 and DE430 is the inclusion of Moon's core and mantle interaction and its effect on its orbit around the Earth as well as the introduction of MESSENGER missions in DE430. In this validation, the Earth Moon interaction and the MESSENGER mission are not included so the settings are identical to the one of DE423.

Table 3.1 provides the observation settings that is used for validation. These settings are directly derived from actual missions observation schedules that are used by JPL to produce their ephemerides. The post-fit residuals plots provided in (Folkner et al., 2014) and INPOP's planetary database [1] were used as the main guideline to get a rough estimate of frequency of the observations for each mission as well as a realistic noise budget. The post-fit residuals plots are not repeated in this thesis however, the reader can compare the values of Table 3.1 and the observation frequency plots and values provided by (Folkner et al., 2014) for verification.

[1] http://www.geoazur.fr/astrogeo/?href=observations/base

TABLE 3.1: Observation scheduling of each observation link for each planet. Each line represent one observation link (Folkner et al., 2014)

Observation Scheduling				
Planet	*Duration*	*Frequency*	*Type*	*μ and σ of the noise*
Mercury	1980 to 1986	80 Obs per 180 days repeated every year	Direct radar	0 ±2 km
	1986 to 1998	15 Obs per 90 days repeated every year	Direct radar	0 ±2 km
	2008 to 2009	1 Obs per year repeated every year	MESSENGER radio	0 ±25 m
Venus	1980 to 1983	50 Obs per year days repeated every year	Direct radar	0±2 km
	1986 to 1996	6 Obs per 7 days repeated every year	Direct radar	0±2 km
	1990 to 1995	3 Obs per 1 day repeated every year	Magellan VLBI	2±4 mas
	2006 to 2010	6 Obs per hour repeated every week	VEX radio	0 ±15 m
Mars	1980 to 1983	18 Obs per hour repeated every month	VIKING radio	0 ±20 m
	1997 to 2010	6 Obs per hour repeated every 4 days	MRO, MO & MEX radio	0 ±5 m
Jupiter	1992	1 flyby observation	Ulysses radio	0 ±100 m
	2001	1 flyby observation	Cassini radio	500 m ±2 km
	1996 to 1998	4 Obs per day every month	Galileo VLBI	5 ± 15 mas
	1980 to 2010	35 Obs per 3 months every half a year	Direct astrometic	0 ±250 mas
Saturn	1980 to 1982	1 Obs per year repeated every year	Voyager radio	250 ±250 m
	2004 to 2010	3 Obs per hour repeated every month	Cassini radio	0 ±50 m
	1985 to 1998	150 Obs per half year repeated every half year	Direct astrometric	0±250 mas
	1998 to 2010	450 Obs per half year repeated every half year	Direct astrometric	0 ±250 mas
Uranus	1980 to 1995	6 Obs per hour every 3 months	Direct astrometric	0 ±250 mas
	1995 to 2010	400 Obs per half year repeated every half year	Direct astrometric	0 ±250 mas
	1986	1 flyby observation	Voyager radio	0 ±100 m
Neptune	1980 to 1995	6 Obs per hour every 3 months	Direct astrometric	0 ±250 mas
	1995 to 2010	300 Obs per half year repeated every half year	Direct astrometric	0 ±250 mas
	1989	1 flyby observation	Voyager radio	0 ±10 m

To ensure the converged results match the one from JPL's model, one needs to ensure that the dynamical models that are used in this thesis closely represent the one of JPL and the simulation time frame is similar. The dynamical models are quite similar to one another with a number of differences which are explained as follows.
The first one is that in JPL's model, 343 asteroids are individually propagated and estimated while this is impossible to do in this thesis due to computational limits. Therefore, this is compromised by including a ring and only propagating the 11 of most optimum asteroids. As was explained in Section 2.3, in theory the combination of the ring and the individual asteroids should cover nearly 90 % of the asteroid belt's perturbation but it would be ideal to individually estimate all 343 asteroids to eliminate any possible differences.

Apart from the asteroids, one other difference is that the position of the Earth and Moon are not among the parameters that are estimated however, they are included in the model and their positions are directly integrated based on the initial conditions provided by JPL's DE423 model. Another difference is the duration of the estimation. In JPL's model, the estimation starts in 1969 and last until 2050 while including all missions observations until 2010 but this was not possible to do in this thesis due to limited

available memory to run the simulation. Hence validation is done from 1980 to 2015. This time period is selected since most of the significant missions are included during this time period which means the biggest effects on the planetary ephemerides can be captured and compared for validation. No a-priori uncertainty are used to regularize the validation at the start of the estimation and the reason for this is the abundance of observation at the beginning of the estimation period which provide a good constraint for the orbits. Having no a-priori uncertainty eliminates the error due to poor selection of a-priori value as this value is not very straight forward to determine for each planet. Hence estimation will purely estimate the parameters based on the available observations.

The error in planets range are shown in the following figures for each of the estimated planets. The uncertainties that are produced in this validation are errors that are computed based on what was explained in Section 2.1.1 and are compared to uncertainties given in (Folkner, 2010) which represent the formal errors of JPL's estimation results. It was decided to only use Gaussian noise on the observation for this validation which will result in errors produced in this validation to closely represent the formal errors of the estimation.

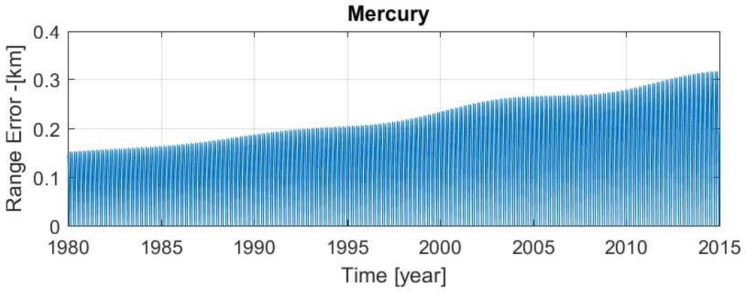

(A) Mercury range error determined during validation process. Computed by subtracting estimated states from states of truth model

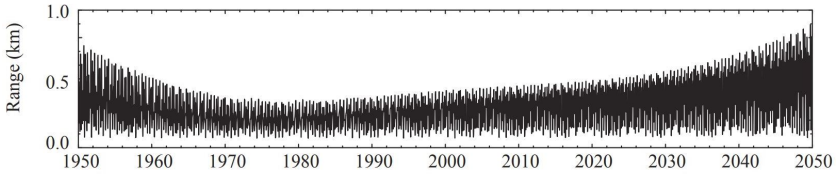

(B) Mercury formal range error estimated in JPL DE423 model (Folkner, 2010)

FIGURE 3.1: Comparison between Mercury's range error. The one computed in this thesis with the one provided by JPL's DE423 model

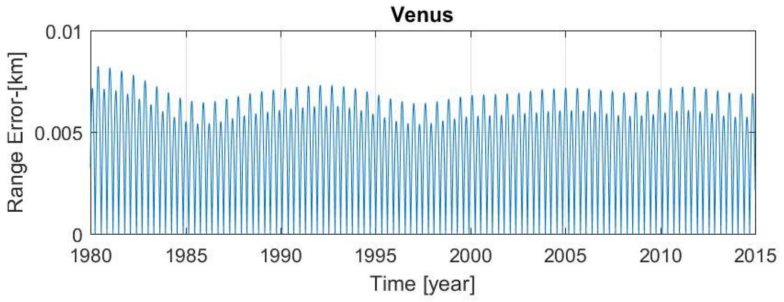

(A) Venus range error determined during validation process. Computed by subtracting estimated states from states of truth model

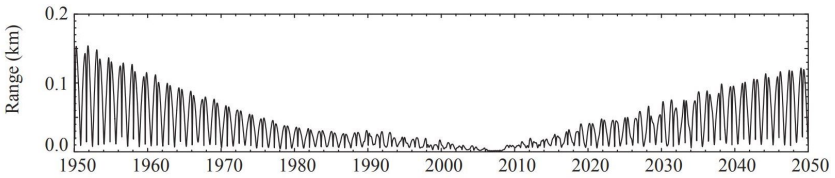

(B) Venus range error estimated in JPL DE423 model (Folkner, 2010)

FIGURE 3.2: Comparison between Venus's range error. The one computed in this thesis with the one provided by JPL's DE423 model

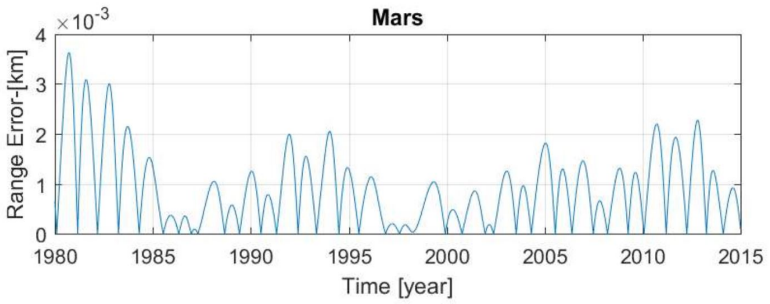

(A) Mars range error determined during validation process. Computed by subtracting estimated states from states of truth model

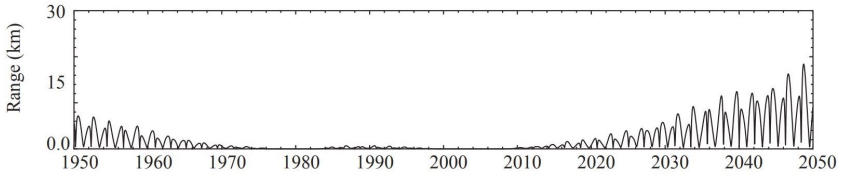

(B) Mars range error estimated in JPL DE423 model (Folkner, 2010)

FIGURE 3.3: Comparison between Mars's range error. The one computed in this thesis with the one provided by JPL's DE423 model

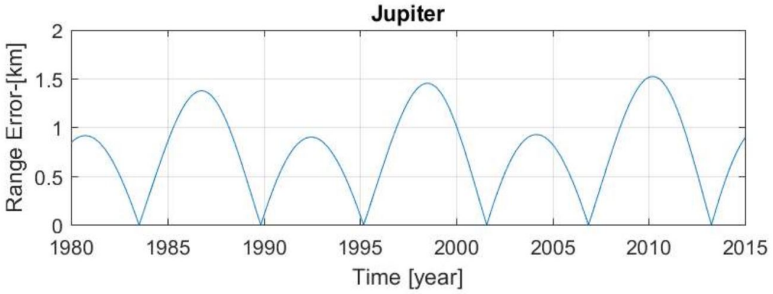

(A) Jupiter range error determined during validation process. Computed by subtracting estimated states from states of truth model

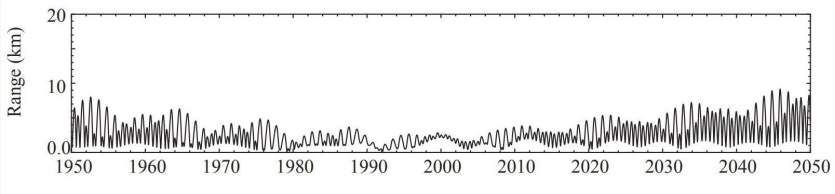

(B) Jupiter range error estimated in JPL DE423 model (Folkner, 2010)

FIGURE 3.4: Comparison between Jupiter's range error. The one computed in this thesis with the one provided by JPL's DE423 model

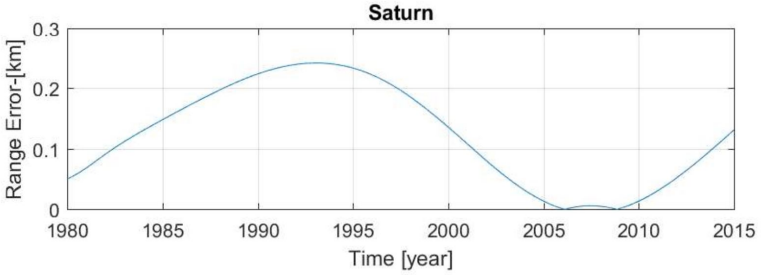

(A) Saturn range error determined during validation process. Computed by subtracting estimated states from states of truth model

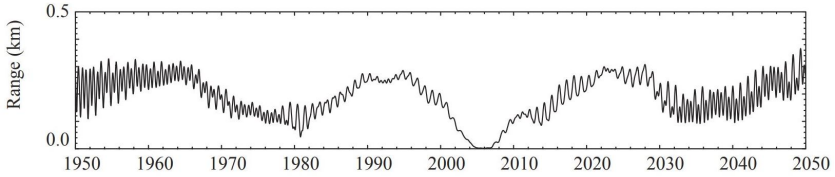

(B) Saturn range error estimated in JPL DE423 model (Folkner, 2010)

FIGURE 3.5: Comparison between Saturn's range error. The one computed in this thesis with the one provided by JPL's DE423 model

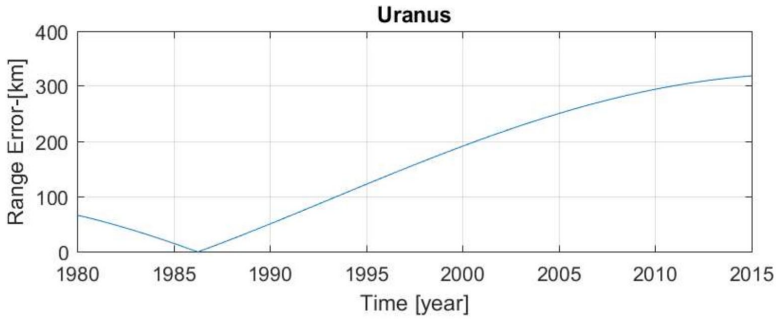

(A) Uranus range error determined during validation process.Computed by subtracting estimated states from states of truth model

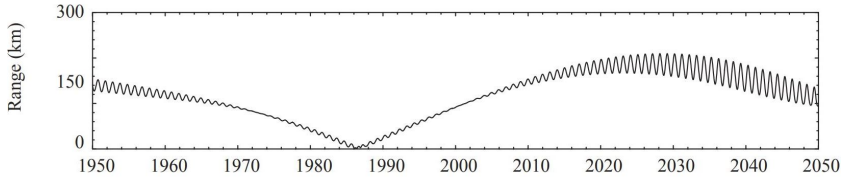

(B) Uranus range error estimated in JPL DE423 model (Folkner, 2010)

FIGURE 3.6: Comparison between Uranus's range error. The one computed in this thesis with the one provided by JPL's DE423 model

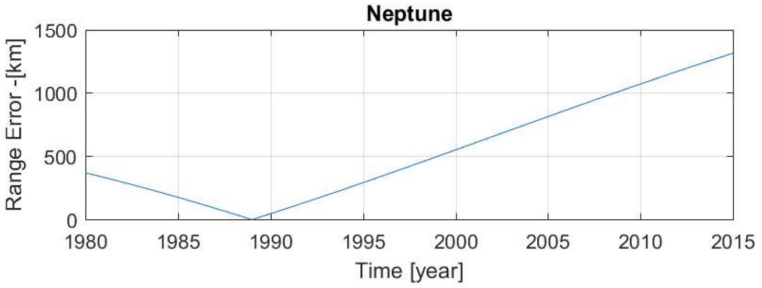

(A) Neptune range error determined during validation process. Computed by subtracting estimated states from states of truth model

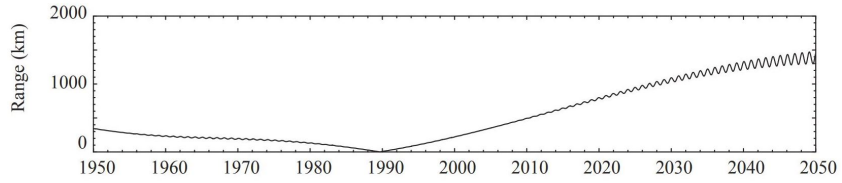

(B) Neptune range error estimated in JPL DE423 model (Folkner, 2010)

FIGURE 3.7: Comparison between Neptune's range error. The one computed in this thesis with the one provided by JPL's DE423 model

As can be seen from the Figures provided in this Section, how the uncertainties produced in this thesis compared to the state of the art uncertaities can be answered. It can be seen that the validation is not perfect but the overall magnitude and behaviour of the uncertainty are quite similar. Venus's magnitude of uncertainty seems to be underestimated which might show that the observation uncertainty budget selected for that planet could have been slightly over optimistic. The outer planets uncertainty are

captured more accurately which could be attributed to the fact that their observation schedule and uncertainty were reproduced properly. There are certain effects that are not being captured in the virtual reality such as the short period variations in the outer planets position. This could be attributed to the fact that the Earth and Moon themselves are not being estimated or not estimating all 343 individual asteroids. Also in this validation, simulated observation directly to planets surface with artificial Gaussian noise level is used. This is not a very realistic representation of reality as actual observations are sometimes made of a planet's Moon or an orbiter around it which adds additional errors in the observation. All in all, these differences are expected to be minimized if one corrects for the aforementioned discrepancies between the dynamical models as well as using actual observations with actual noise budget.These discrepancies could also result in the results in Figures provided here differ with one another.

The question of whether having a truth and estimation model as a mean to asses the uncertainty is valid or not is answered positively because the errors that are produced in this validation are not the estimation formal errors but the difference between the estimated parameter and the states from a reference truth model. Given that these uncertainties very well represent the formal errors of the state of the art ephemerides generation models shows that this method of assessing the error is certainly a valid way. In other words. the process of having a virtual reality (or a truth model) as a reference point to compare the estimated results to in order to asses the performance of the estimation seems to be a valid process. Hence, there is no need to solely rely on estimation's formal error compute the planetary uncertainties and avoid the problem of having overly optimistic results and also eliminates the need of formal error propagation and assumptions that comes with it.

The question of whether using internally simulated observations instead of actual ones is valid or not is also answered positively as these results are produced without using any observations from actual missions. All the observations are simulated internally and appropriate noise levels are applied on top of them to reenact what is happening in reality. Yet the results are capable of slightly matching the ones where actual observations are used.

All in all, the overall approach and the ephemerides generation process introduced in this thesis is validated and is ready for testing any hypothesis regarding interplanetary laser ranging or any other hypothesis for that matter (more on other possible studies that can be done using this model is provided in Chapter 5)

3.2 Validation of asteroid ring model

To validate whether the implemented ring model (see Section 2.7) in this thesis is done correctly and is in line with what was explained by (Kuchynka et al., 2010), the perturbation on Earth-Mars distance due to the presence of the ring is plotted over 30 years and compared to the results provided by (Kuchynka et al., 2010). The ring's radius is selected to be 2.8 AU and its mass to be $0.34 \times 10^{-10} \times M_{sun}$ which is exactly the values used to produce Figure 3.8a in (Kuchynka et al., 2010). Figure 3.8 shows this comparison and one can see that the results are inline with one another.

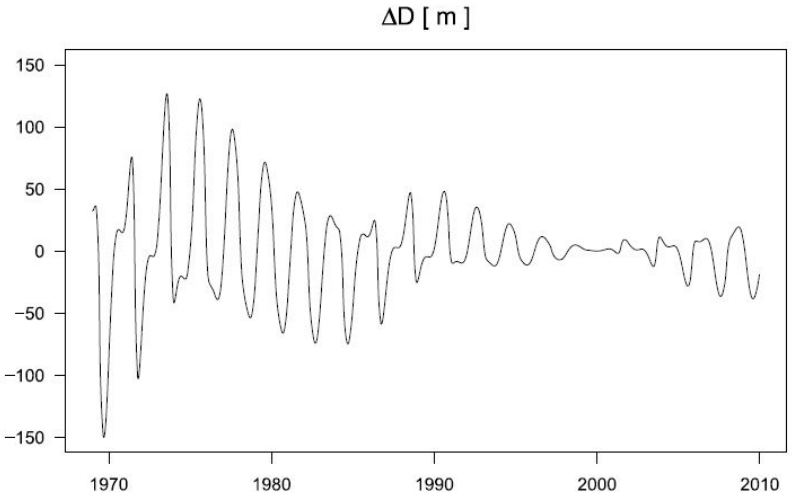

(A) Earth-Mars perturbation due to presence of a ring with $M_{ring} = 6.726 \times 10^{19}$ at 2.8 AU distance provided by (Kuchynka et al., 2010)

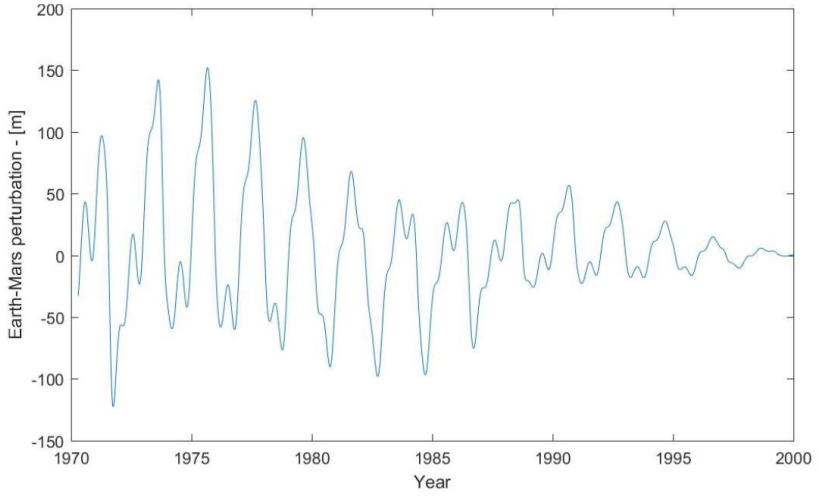

(B) Earth-Mars perturbation due to presence of a ring with $M_{ring} = 6.726 \times 10^{19}$ at 2.8 AU distance computed in this thesis

FIGURE 3.8: Validation of ring model implemented in this thesis

There are a number of remarks that should be made about the ring model that is implemented in this thesis. Firstly, the interaction between the ring and the solar

system bodies are only one-sided. Meaning the mutual acceleration of the other bodies on the ring is not accounted for. This causes the solar system's momentum to become non-conservative since external momentum is being added to the system which results in the barycenter of the solar system to shift by a 10 meters over the course of 100 years (Kuchynka et al., 2010). This is not a big issue for short term simulations like the one performed here however, it is recommended to account for this if one requires long term interplanetary orbit propagation. Hence it is recommended to have ring's position as a non-fixed parameter in which it changes under the influence of mutual acceleration of other bodies in the solar system to conserve the system's momentum. This could explain the existence of small differences that is seen in Figure 3.8.

3.3 Systematic noise validation & its effect on the estimation results

The systematic noise profile which is induced on the observations attempts to ensure that a time dependent noise signature which in reality cannot be corrected for is present during the estimation to result in more realistic results (as was explained in Section 2.6.1). In this Section the induced noise profile on the observations as well as the effect that it has the post-fit residuals and converged solution of the problem are shown. This gives an insight on how sensitive are the estimated orbits to the profile of the noise as well as give some ideas on the reliability of the noise function purposed in Section 2.6.1.

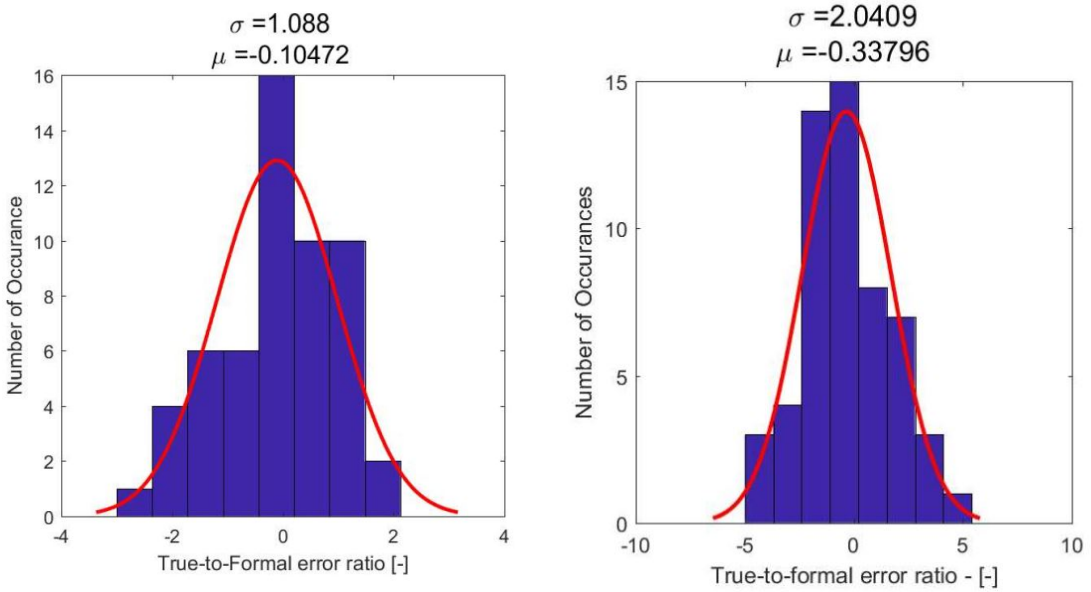

(A) True to formal error ratio histogram for all the 55 estimated parameters with only stochastic noise

(B) True to formal error ratio histogram for all the 55 estimated parameters with both stochastic and systematic noise

FIGURE 3.9: Comparison of true to formal error distribution with and without systematic noise profile

The effect of systematic noise profile can be directly seen from the post-fit residuals of the observation of each link end as well as the true error of the estimation. Figure 3.9 shows how the true to formal error distribution changes for all estimated parameters when systematic noise profile is introduced to the estimation. The induced systematic noise profiles for each linkend is shown in Figure 3.10. These results are produced using the same settings that were used to produced the results shown in Chapter 4.

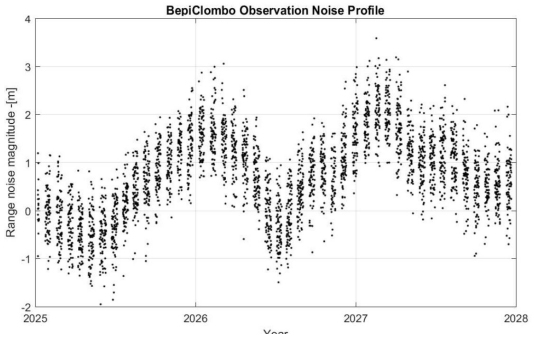

(A) The noise profile that is put on the BepiClombo's range observations

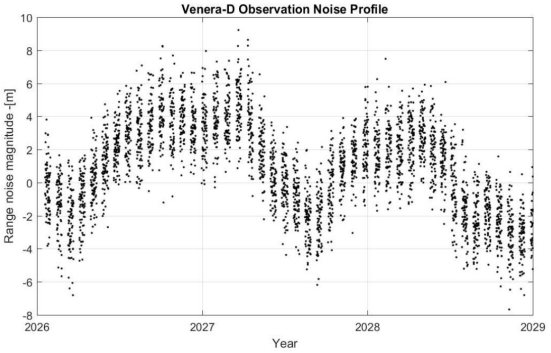

(B) The noise profile that is put on the VeneraD's range observations

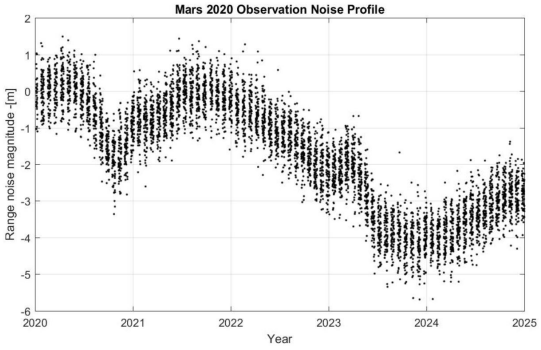

(C) The noise profile that is put on the Mars's range observations. (all missions in Table 2.3 are combined under one mission Named Mars 2020)

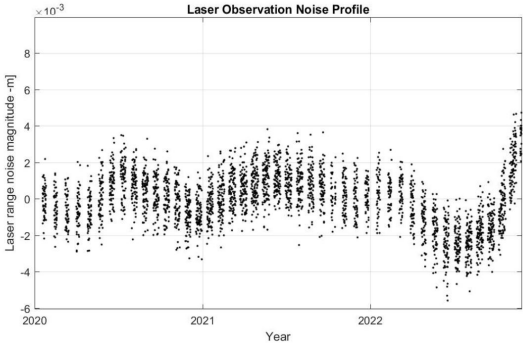

(D) The noise profile that is put on the Mars's laser range observations

FIGURE 3.10: The systematic noise profile that is put on the observations

The systematic noise causes the true error of most of the parameters to deviate by a factor in the vicinity of 2 from the formal error. For instance, true to formal ratio of inner planets' position error are 1.4, 3.8 and 1.8 for Mercury, Venus and Mars respectively. The ratios for velocity of these planets are 1.5, 1.9 and 2.1 respectively which are all in agreement with what is suggested by literature for interplanetary ephemerides (Folkner, 2010). Some of the parameters deviate as large as a factor of 4 to 5, notably the Venus and asteroid masses, while some other parameters show a ratio closer to one. These values are not out of ordinary as they very much depend on the noise profile that is put on the specific linkends. Of course the ratios suggested by the literature are not strict rules but merely a rough suggestions to give an idea of how realistic formal errors are with respect to what is actually happening in reality. The fact that the true to

formal error ratio that is displayed here does not exceed the ones suggested from the literature and is in agreement with them is indicative of the systematic noise profile to be a reliable method for producing realistic estimation results.

In other words, the induced systematic noise is carefully selected such that it includes short and long term variation of noise while maintaining a true to formal error ratio that is within the realms of what is suggested by the literature. This means that the noise profile does not cause the true error or the estimation results to significantly deviate from the case when they are not used while at the same time, its effect is not negligible either.

From Figures 3.10 it can be seen that the systematic noise is only put on the range observations made to the interplanetary orbiters or landers and not on the astrometic or direct observations made to the planets. As was also explained in Section 2.4.2, This is done by analyzing noise budget and post-fit residuals of various missions and link-ends as well as looking at literature to get an idea of which linkends are relevant for having systematic noise behaviour. It was observed that observations to interplanetary orbiters or landers (especially range observations) typically show a time dependent noise behaviour due to their high observation frequency, presence of clock biases, atmospheric delays and so on and so forth which typically result a systematic noise signature on the observations that are not managed to be corrected for (Viswanathan et al., 2017), (Folkner et al., 2014). Direct astrometric observations that are typically done to outer planets are largely dominated by stochastic noise as they are typically so infrequent that do not show any time dependent noise behaviour. Based on those observations, only the linkends shown in Figure 3.10 are selected to have uncorrected and time dependent systematic noise while for the rest of the observations' noise profile is selected to be Gaussian.

The effect of systematic noise on the post-fit residuals is also interesting to analyze. A comparison between post-fit residuals of the linkends with and without systematic noise is provided below

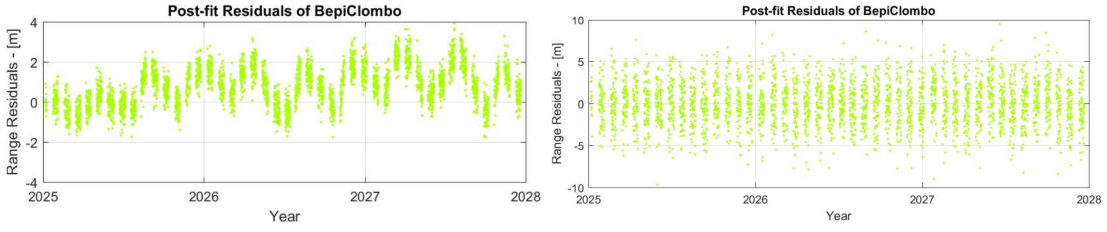

(A) Mercury's Bepiclombo range residuals with systematic noise

(B) Mercury's Bepiclombo range residuals without systematic noise

FIGURE 3.11: Comparison of Post-fit residuals of Mercury linkend with and without systematic noise

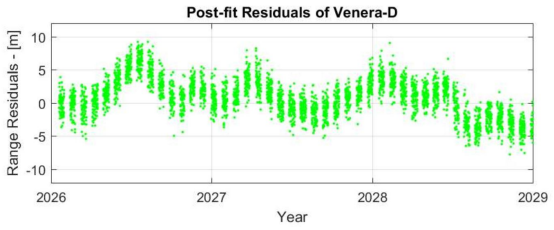

(A) Venus's Venera-D range residuals with systematic noise

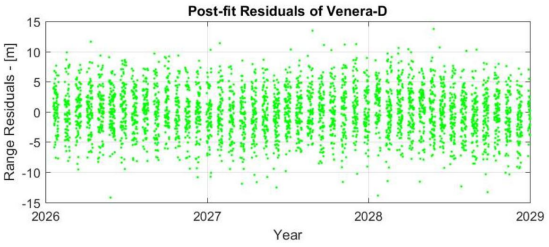

(B) Venus's Venera-D range residuals without systematic noise

FIGURE 3.12: Comparison of Post-fit residuals of Venus's range linkend with and without systematic noise

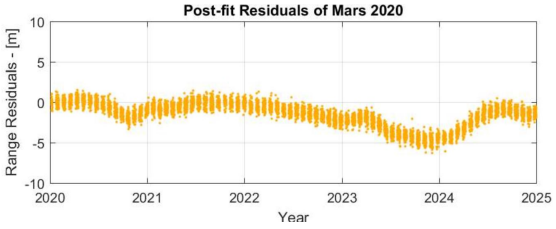

(A) Mars's Mars2020 range residuals with systematic noise (all missions in Table 2.3 are combined under one mission Named Mars 2020)

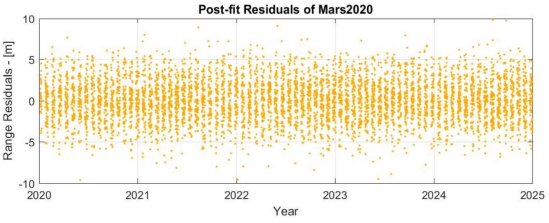

(B) Mars's Mars2020 range residuals without systematic noise (all missions in Table 2.3 are combined under one mission Named Mars 2020)

FIGURE 3.13: Comparison of Post-fit residuals of Mars's range linkend with and without systematic noise

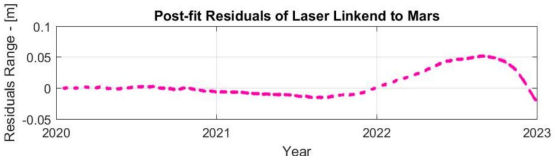

(A) Mars's hypothetical laser range residuals with systematic noise

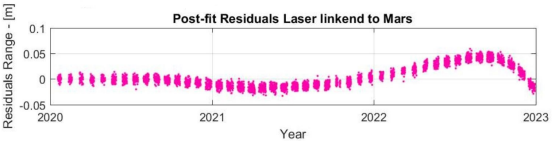

(B) Mars's hypothetical laser range residuals without systematic noise

FIGURE 3.14: Comparison of Post-fit residuals of Mars's hypthetical laser linkend with and without systematic noise

Judging by the post-fit residuals of the estimation, it can be seen that the induced systematic noise profile is clearly dominating the shape of the post-fit residuals, except for the laser linkend. Without systematic noise however, the residuals are simply converged to the stochastic noise level that was put on the observations.

One interesting observation is the post-fit residuals of the laser linkend which seems to be unchanged by the introduction of systematic noise. It seems that the laser ranging linkend is dominated by not the observation uncertainty of that linkend but the uncertainty in the dynamical parameters of the estimation, either the uncertainty in planets states or the asteroid masses. This is expected as the laser observations are selected to have a few millimeter level uncertainty while the solution to the observation equation of this linkend with all the estimated parameters does not come close to this level of

precision as many of the parameters in the observation equation are uncertain to much higher levels. This causes the residuals to take shape of those uncertain parameters which have the largest effect on this linkend. It can be speculated that this particular shape is related to the uncertainty in Mars's estimated position which is estimated with centimeter level accuracy while the observation uncertainty is at millimeter level causing a deviation between the computed observation equation and the provided observation accuracy. This is where the dynamical coupling between all the estimated parameters are displayed which shows how laser ranging attempts to minimize the uncertainty in all the estimated parameters as best as it can and it absorbs their effects. The estimated uncertainty of the asteroid masses could also be the reason for this shape as they show very high sensitivity to the laser ranging linkend which are displayed in Figure 4.18.

All in all, the results that are displayed in this section show that the systematic noise function that was developed in Section 2.6.1 can be a good enough method to ensure the estimation environment reenact the reality to a certain extend. The true to formal error ratio looks realistic and inline with what is suggested from literature and the behaviour of the uncertainties are not drastically changed. One can still perform the estimation using purely Gaussian noise profile for all linkends but it has to be remembered that will result in true errors to resemble formal errors and ultimately result in overly optimistic error values which was exemplified in Table 4.2.

Chapter 4

Results & Discussion

In this Chapter the results of the simulation that uses all the models and settings explained in Chapter 2 are shown and discussed. This Chapter compares the results of two cases both performed between 2020 and 2050 with identical settings described in Chapter 2 and observation schedules shown in Table 2.4. The only difference between the two cases is that in one of the cases laser ranging to Mars is activated between 2020 to 2023. Planetary ephemerides, estimated asteroid masses, dynamical and relativistic asteroid masses are estimated in both cases in an attempt to answer the research question provided in Section 1.2.

The layout of this Chapter is as follows. In Section 4.1, the effect of laser ranging on the planetary ephemerides themselves are looked at and the differences are noted. The comparison between the estimated asteroid masses as well as the estimated dynamical and relativistic parameters for two cases are provided in Sections 4.2 and 4.3 respectively to quantify the effect of laser ranging on these parameters as well.

4.1 Laser ranging effect on planetary orbital parameters

The true error in position and range for the two cases are compared in this Section. The concept of how this true error is computed and how it differs from the formal estimation error is shown in Section 2.1.1. These true errors are computed using the following relations in which $\bar{r}_{i,vr}$ represents the position vector of i^{th} planet computed in virtual reality model (i.e truth model). Similarly, $\bar{r}_{i,est}$ represent the position vector of i^{th} planet computed in the estimation model for both cases with and without laser ranging.

$$\delta\rho_i = |\bar{r}_{(i,est)}| - |\bar{r}_{(i,vr)}| \tag{4.1}$$

$$\delta\bar{r}_i = |\bar{r}_{(i,est)} - \bar{r}_{(i,vr)}| \tag{4.2}$$

The difference between Equations 4.1 and 4.2 are distinctive as the former represent the error in the planet's range while the latter shows the global position error of the planet. The reason why these two errors are looked at independently is because laser ranging is capable of providing very precise constraints on the planet's range specifically and not so much on planet's declination or right ascension. It is important to denote the difference between the two when one is talking about the implementation of interplanetary laser ranging as it is a much more valuable scientific return if one is able to identify exactly which components of the orbital elements are improved drastically with the introduction of laser ranging. Hence looking at range error will provide an additional and a better insight on the effect of the laser ranging on components of the orbit in which it is expected to improve the most.

By looking at $\delta\rho_i$ and $\delta\bar{r}_i$ of the two cases, one can get an idea on how much improvement in planetary position is expected when laser ranging is introduced. First the comparison of the global position error are displayed for all the estimated bodies in the Figures below. In this Figures, the red line represent the error for the case with laser ranging to Mars while the blue line represent the error for the case without laser ranging to Mars.

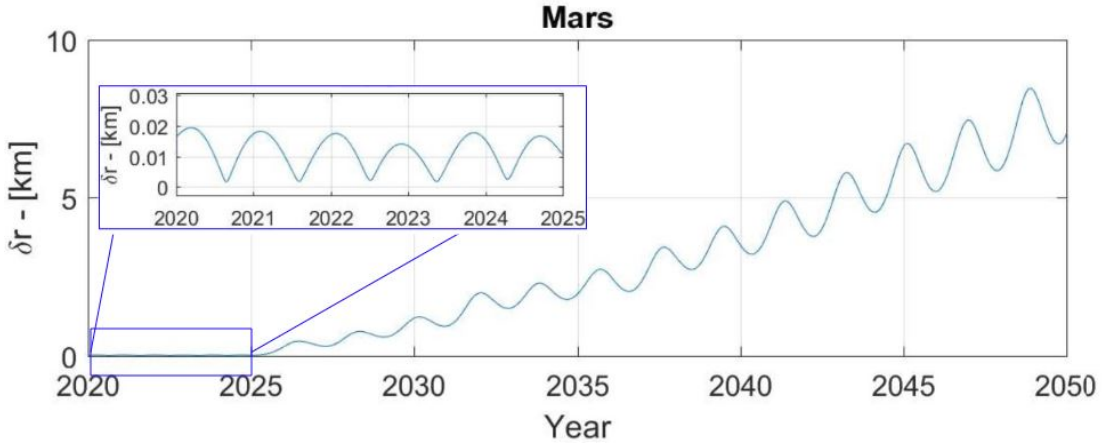

(A) Error in Mars's position vector without utilizing laser ranging to Mars

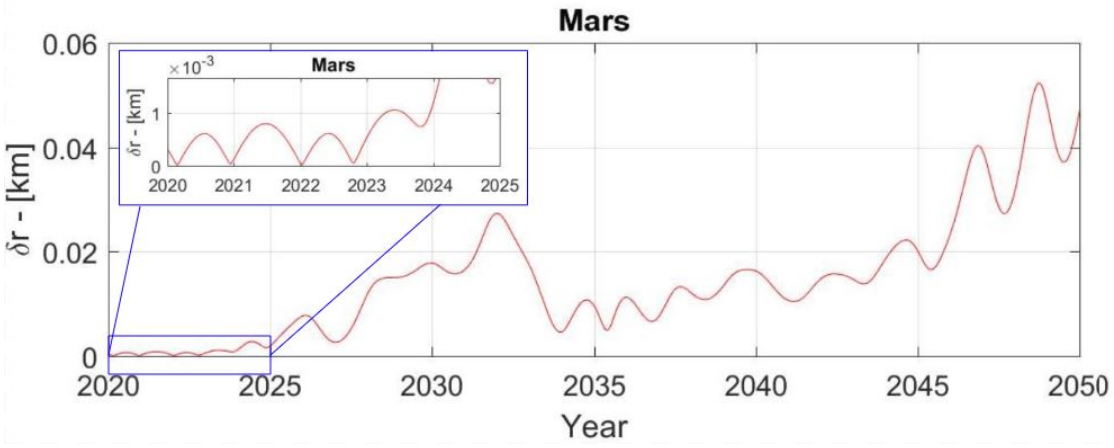

(B) Error in Mars's position vector for the case where laser ranging to Mars is utilized

FIGURE 4.1: Comparison of position error of Mars between the two cases of utilizing (Red line) and not utilizing laser ranging to Mars (Blue line)

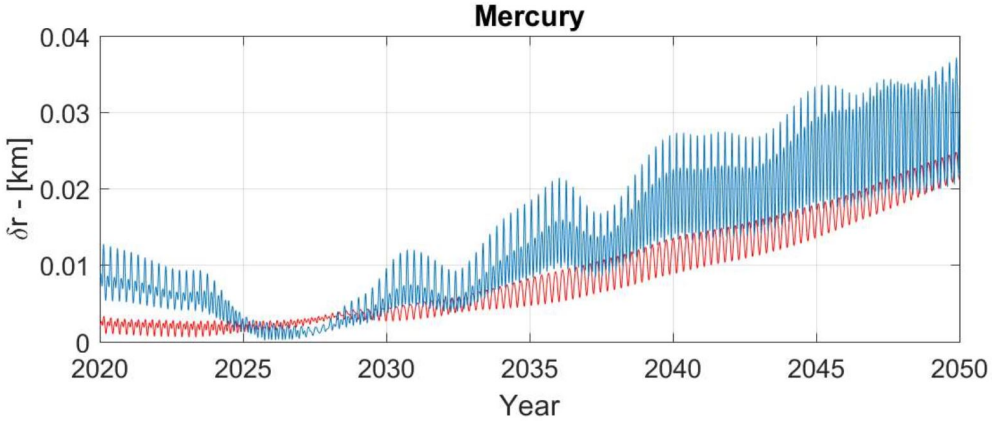

FIGURE 4.2: Comparison of position error of Mercury between the two cases of utilizing (Red line) and not utilizing laser ranging to Mars (Blue line)

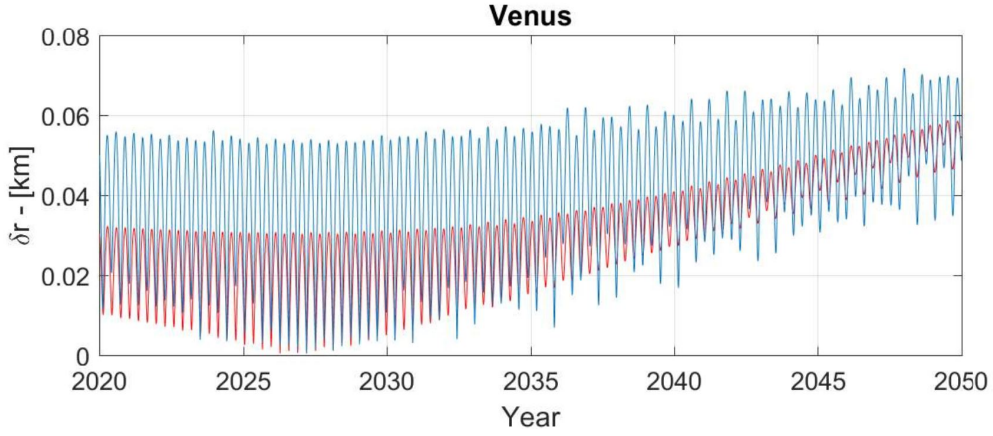

FIGURE 4.3: Comparison of position error of Venus between the two cases of utilizing (Red line) and not utilizing laser ranging to Mars (Blue line)

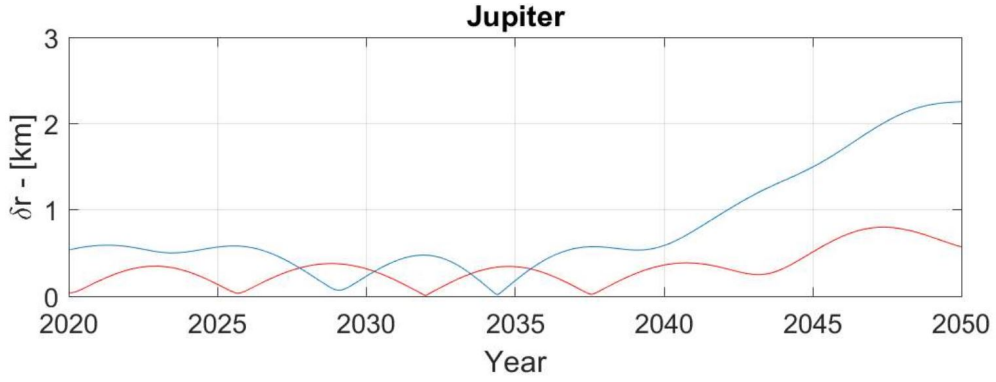

FIGURE 4.4: Comparison of position error of Jupiter between the two cases of utilizing (Red line) and not utilizing laser ranging to Mars (Blue line)

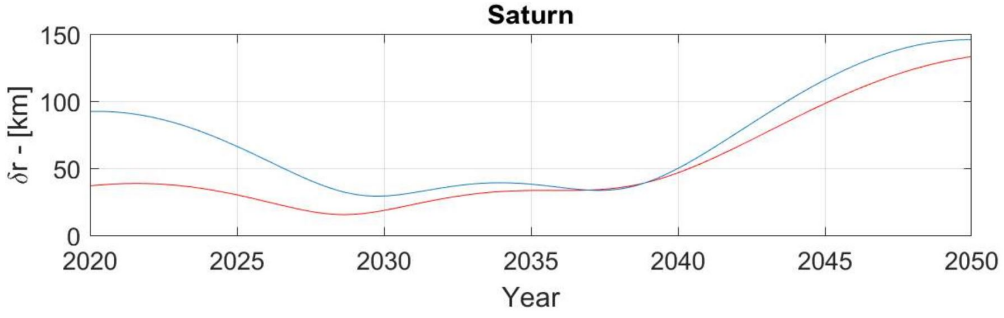

FIGURE 4.5: Comparison of position error of Saturn between the two cases of utilizing (Red line) and not utilizing laser ranging to Mars (Blue line)

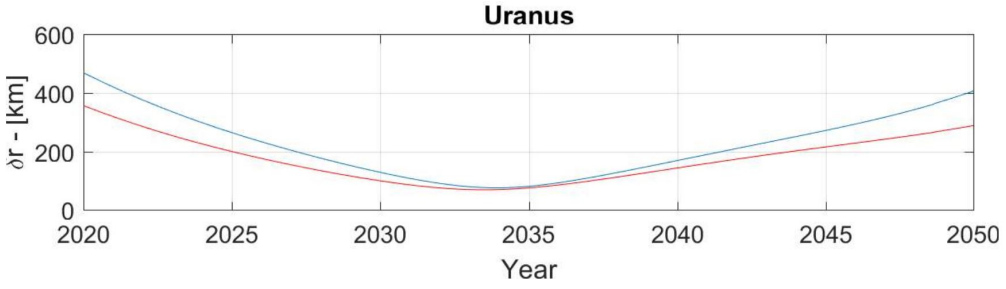

FIGURE 4.6: Comparison of position error of Uranus between the two cases of utilizing (Red line) and not utilizing laser ranging to Mars (Blue line)

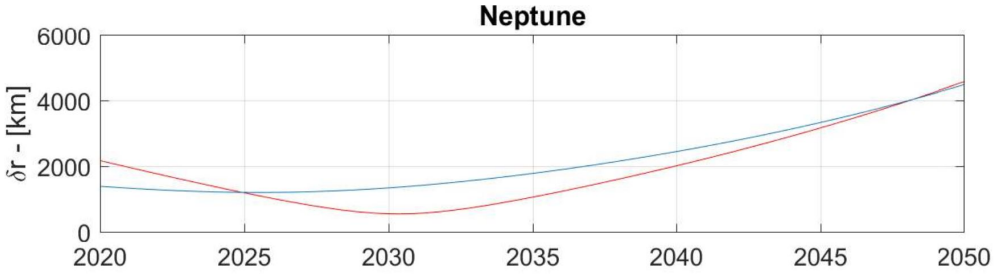

FIGURE 4.7: Comparison of position error of Neptune between the two cases of utilizing (Red line) and not utilizing laser ranging to Mars (Blue line)

The comparison of the range error for all the estimated bodies are are displayed in Figures below.

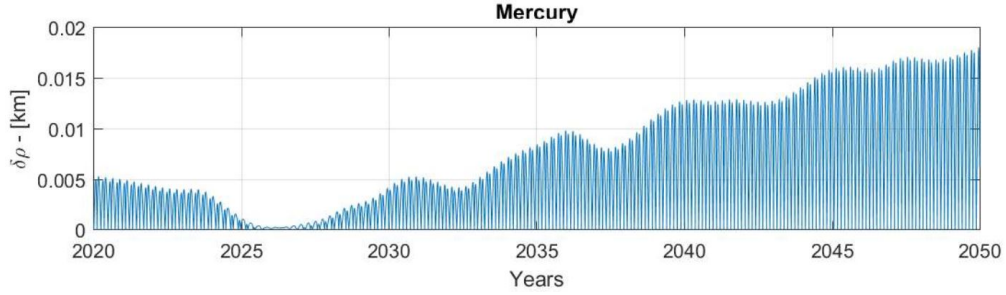

(A) Error in Mercury's range without utilizing laser ranging to Mars

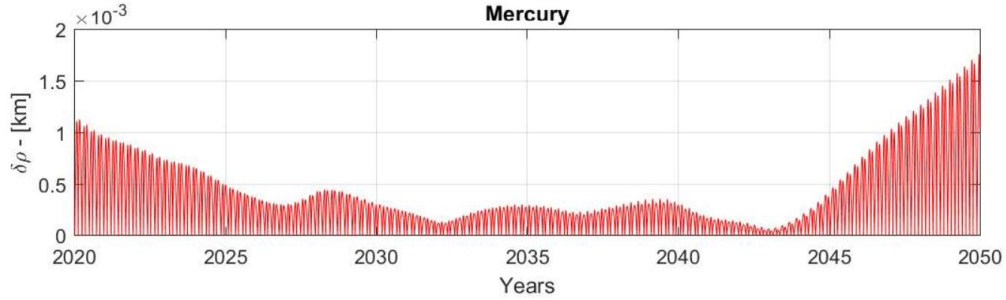

(B) Error in Mercury's range for the case where laser ranging to Mars is utilized

FIGURE 4.8: Comparison of range error of Mercury between the two cases of utilizing (Red line) and not utilizing laser ranging to Mars (Blue line)

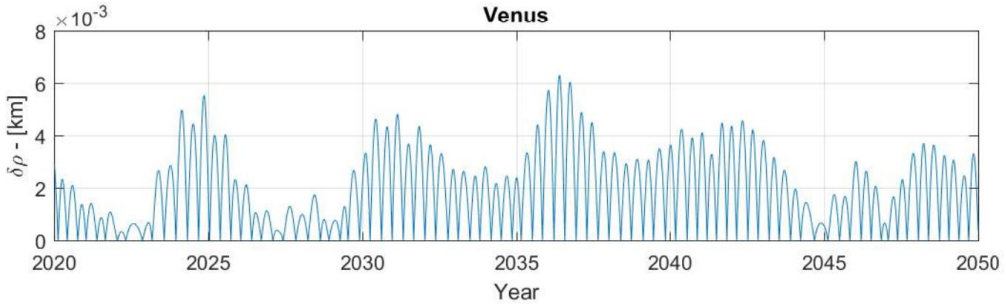

(A) Error in Venus's range without utilizing laser ranging to Mars

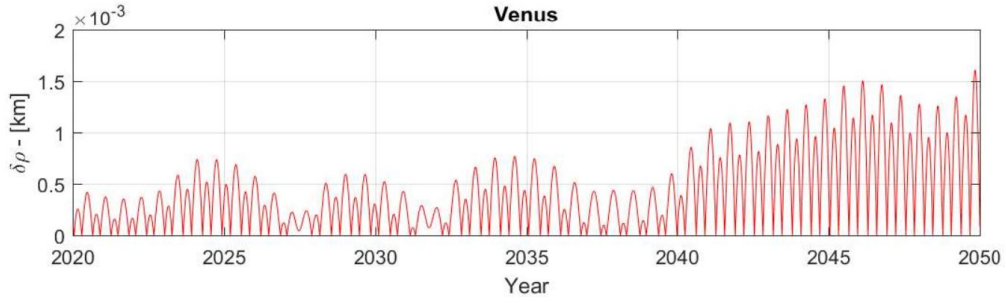

(B) Error in Venus's range for the case where laser ranging to Mars is utilized

FIGURE 4.9: Comparison of range error of Venus between the two cases of utilizing (Red line) and not utilizing laser ranging to Mars (Blue line)

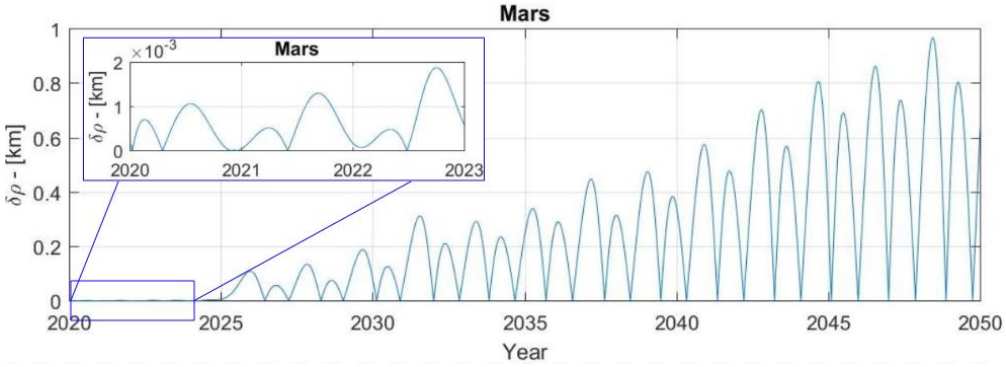

(A) Error in Mars's range without utilizing laser ranging to Mars

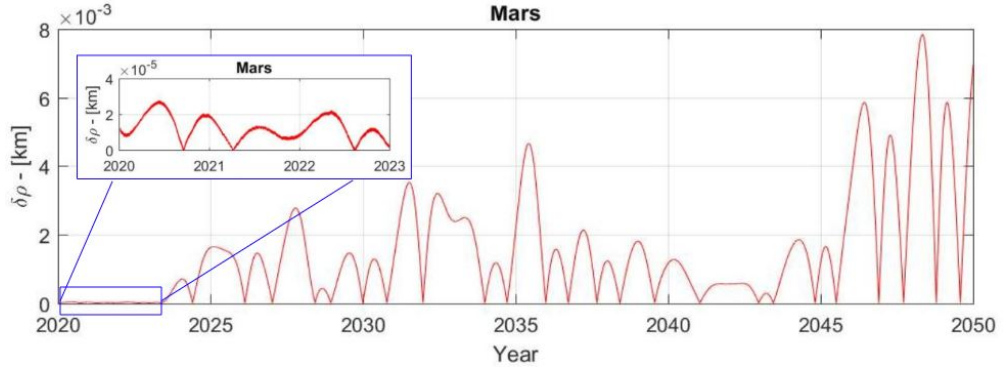

(B) Error in Mars's range for the case where laser ranging to Mars is utilized

FIGURE 4.10: Comparison of range error of Mars between the two cases of utilizing (Red line) and not utilizing laser ranging to Mars (Blue line)

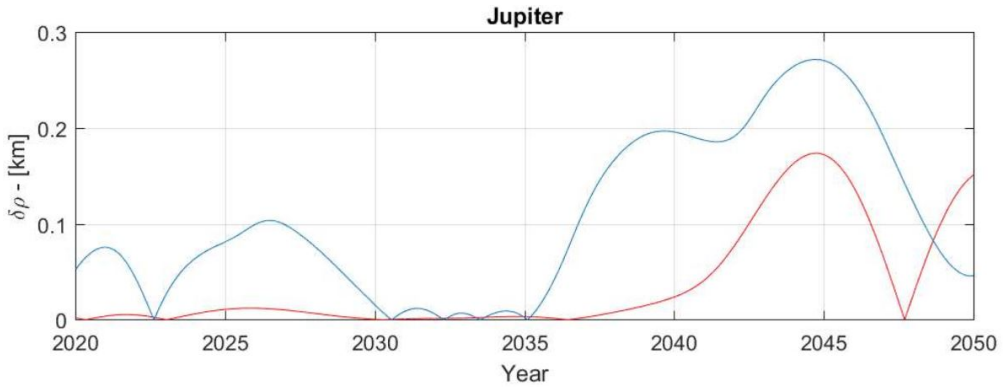

FIGURE 4.11: Comparison of range error of Jupiter between the two cases of utilizing (Red line) and not utilizing laser ranging to Mars (Blue line)

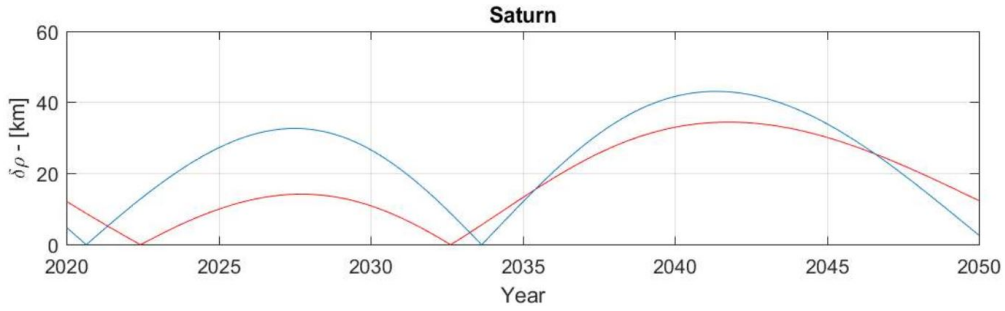

FIGURE 4.12: Comparison of range error of Saturn between the two cases of utilizing (Red line) and not utilizing laser ranging to Mars (Blue line)

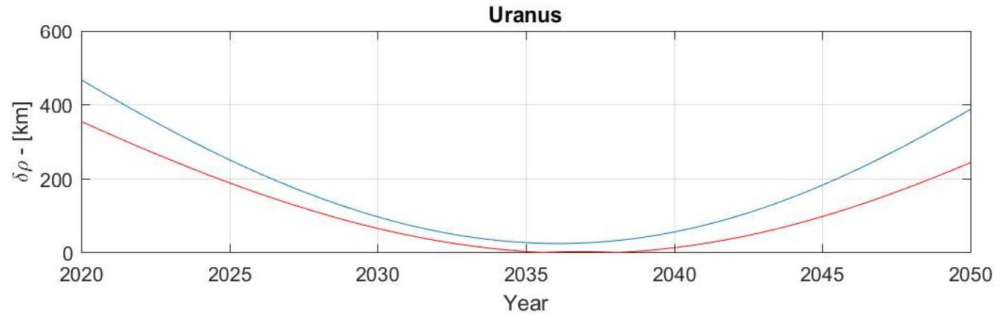

FIGURE 4.13: Comparison of range error of Uranus between the two cases of utilizing (Red line) and not utilizing laser ranging to Mars (Blue line)

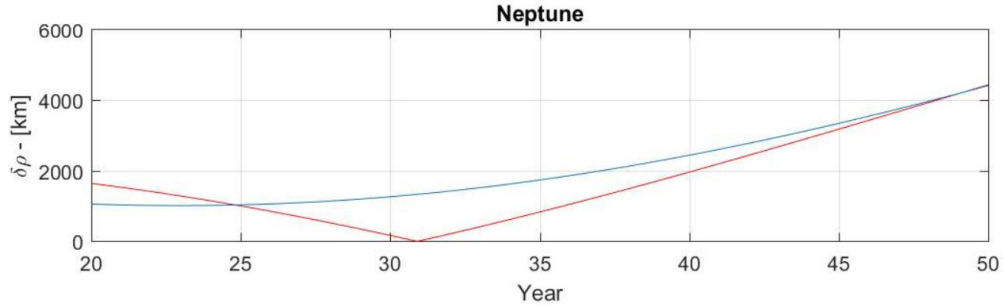

FIGURE 4.14: Comparison of range error of Neptune between the two cases of utilizing (Red line) and not utilizing laser ranging to Mars (Blue line)

From the produced results, a number of observations about the influence of the laser ranging can be made.
First and foremost, Figure 4.10 shows a direct improvement in the orbit of Mars's position vector. One can also see a long term stability of the orbit which can be attributed to two reasons. First is the very precise determination of the initial condition of the Mars's state which means over the long time periods it diverges less compared to a less accurate initial conditions. The second possible factor, is the improvement in the estimated asteroid masses which indirectly effect the long term stability and accuracy of the orbits as the perturbation of the asteroid masses are generally accumulated over long time periods. Improvement in asteroid mass uncertainty is also the reason why the long term accuracy of the Mars's orbit more than any other body in solar system as Mars's orbit is the most sensitive to asteroid belt.

Figure 4.8 also shows that that the achievable range accuracy of Mars during the time where millimeter level laser ranging is available can be reduced to a 2-3 centimeters which is larger than the integration error as was mentioned in Section 2.8. This further validates that the estimation results are not dominated by the integration errors and the selected integrator and integration time step are valid.

The second observations is inline with what was expected and explained earlier in this Section. That is improvement in range uncertainty is much more significant that the improvement in other components of the orbital parameters and is the major contributing factor in improving the global position uncertainty of the planets. Also due to dynamical coupling between Mars, asteroid belts and other major bodies, having improved position knowledge of Mars results in improvements in the position knowledge of other major bodies as well.

The third observation is that laser ranging does not necessarily or consistently contribute to the orbital accuracy of Uranus and Neptune. Because these planets are not very well constraint due to lack of consistent accurate observation and not a long enough observation and simulation timespan to cover their full orbit. This can be seen from

correlation matrices shown Figures 4.15 and 4.16 which indicates the orbital parameters of these vectors to be highly correlated. This ins inline with what is suggested in literature and state of the art ephemerides generation processes (Viswanathan et al., 2017), (Folkner et al., 2014) and the correlation matrix provided by INPOP17 (Verma et al., 2014).
Laser ranging to Mars does not really better constrained these planets' orbits, hence making the conclusion that the orbit of Neptune and Uranus are at the luxury of seeing drastic improvements from laser ranging to Mars is overly optimistic and slightly a premature conclusion at this stage. Uranus seems to see some improvements both in its range and position uncertainty but given that the correlation of Uranus's orbital elements remain high with and without laser ranging, one cannot make a conclusive remark. Given the current constraints that we have of these planets, not much can be said about the influence of laser ranging on these planets. A more conclusive analysis could be performed on the effect of laser ranging on the orbit of these two planets if their orbits planets had better constraints but that is not the case currently or will not be the case in the near future as no missions have been planned to these gas giants.

Looking at correlation matrices given in Figures 4.15 and 4.16, it can be observed that laser ranging to Mars causes elevation of correlation of planetary orbital parameters to Mars which is expected due to dynamical coupling between Mars and other bodies. Not estimating the orbit of Earth takes a toll on the correlation values as one of solar system dynamical coupling chains are eliminated. However, as was mentioned in Section 2.9, not estimating the Earth is equivalent of having very accurate apriori constraints on Earth which will result in Earth's position to be de-correlated from other parameters on the solar system, slightly elevating the interplanetary correlations.

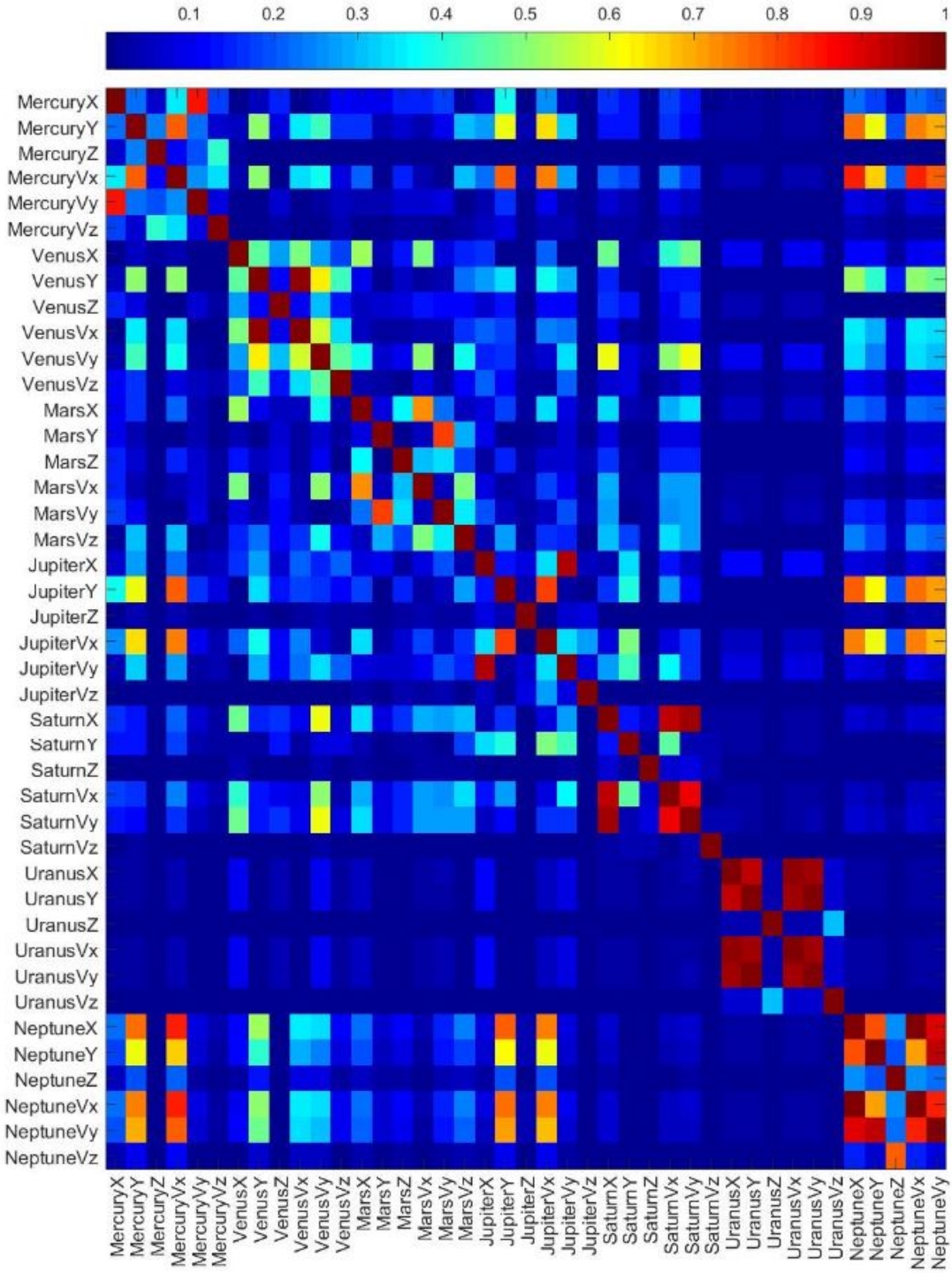

FIGURE 4.15: Correlation between the estimated planetary states for the case without laser ranging

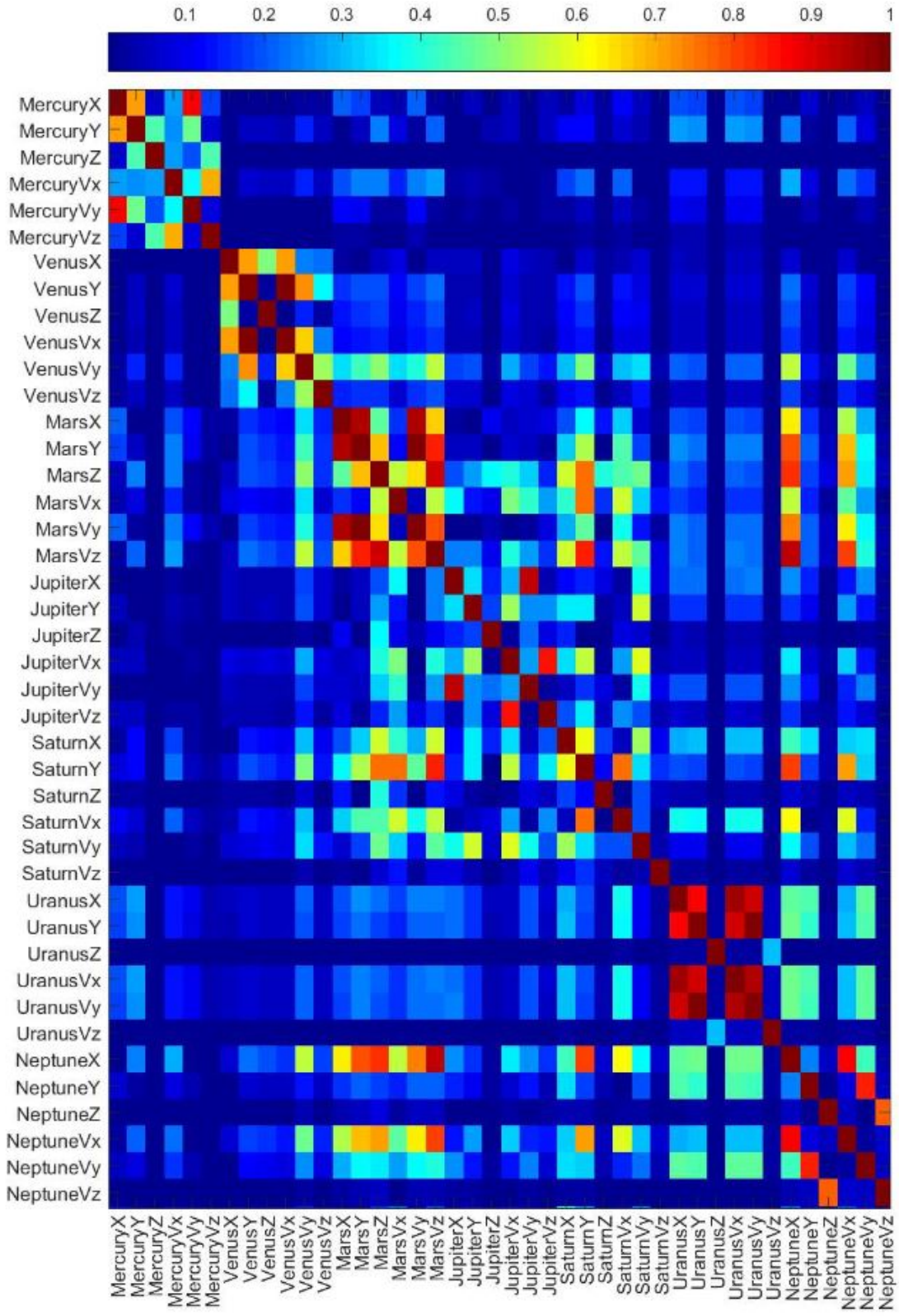

FIGURE 4.16: Correlation between the estimated planetary states for the case with laser ranging

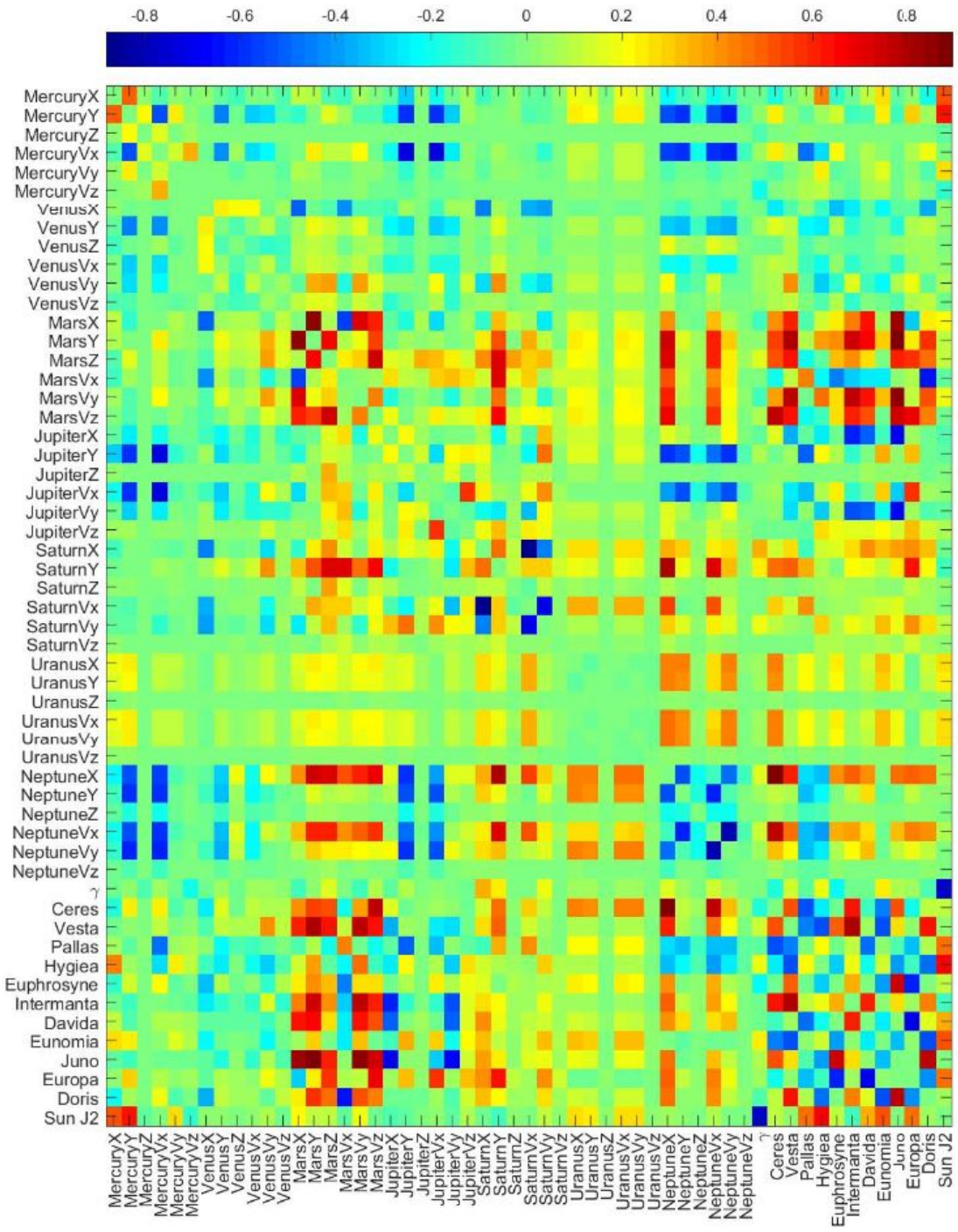

FIGURE 4.17: Full relative correlation matrix which shows the change in correlation values with introduction of laser ranging (i.e $|Corr_{Laser}| - |Corr_{NoLaser}|$)

4.2 Laser ranging effect on asteroid masses

As was mentioned in Section 2.3, the mass of the 11 most optimum asteroids provided in Table 2.2 are estimated alongside the planetary positions. Due to the significant effect of the asteroid belt on the orbit of Mars, laser ranging is expected to provide a significant improvement in the estimated asteroid masses. The estimated asteroid masses are compared between the two cases of with and without laser ranging to Mars to see the extend of the improvement. These values are then compared to the true asteroid mass parameters, the ones from virtual reality (i.e truth model), in order to get a sense of the level of uncertainty that is attached to each individual estimated asteroid mass parameter. These values are shown in Table 4.1.

TABLE 4.1: Comparison between estimated asteroids mass parameter and their true value to get an idea of the relative improvement in asteroid uncertainty with introduction of laser ranging

Asteroid Name	*True* μ_{ast} $[\frac{km^3}{s^2}]$ *from truth model*	μ_{ast} *without LR to Mars* $[\frac{km^3}{s^2}]$	μ_{ast} *with LR to Mars* $[\frac{km^3}{s^2}]$
1 Ceres	63.18	62.73	63.16
4 Vesta	17.74	17.83	17.75
2 Pallas	14.08	13.94	14.05
10 Hygiea	5.84	6.44	5.85
31 Euphrosyne	3.58	2.30	3.53
704 Intermanta	2.60	2.81	2.63
511 Davida	2.56	1.49	2.57
15 Eunomia	2.11	1.72	2.09
3 Juno	1.99	1.50	1.93
52 Europa	1.75	1.54	1.74
48 Doris	1.73	3.03	1.81

It can be noticed that laser ranging to Mars, even for a short period of only 3 years, will result in drastic improvement in the masses of the estimated asteroids. This was expected as asteroids that have been individually estimated here have up to a few kilometers effect on the orbit of Mars over the period of 30 years (Kuchynka and Folkner, 2013) (e.g Ceres and Vesta with an effect of nearly 10 kilometers on orbit of Mars over 30 years). This justifies why 3 year laser ranging allows for significant improvement in knowledge of asteroids. Looking at Table 4.1, it does not become possible to assume that since there 11 asteroids see a large improvement in their mass parameter, the same level of improvement should be expected to be seen for the rest of the asteroids that

are not estimated individually. Since the effects of the rest of the asteroids are much smaller than the ones estimated here and their effects become prominent over longer period of time, hence one cannot tell whether this level of improvement is expected for those asteroids as well. Improvement in all asteroid masses is expected with the current setting but the magnitude of the improvement will for sure differ for each asteroid and it will be a function of their perturbation on the orbit of Mars. As will be explained in Chapter 5, it is highly recommended to perform this simulation while estimating more asteroids individually in the future when the computational budget allows it to get a better idea of the effect of laser ranging on possibly all of the non-negligibly perturbing asteroids in the asteroid belt. Judging by studies performed by (Kuchynka and Folkner, 2013) and the results that have been produced here, it is highly likely that a longer period of laser ranging (maybe close to about 10 years) will probably be required if one wants to achieve a significant improvement in all 343 non-negligible asteroid masses and not just the 11 that are estimated here.

The mass of the ring itself is not estimated. The reason for that is the ring mass is optimally selected to account for the rest of the belts perturbation and its mass is assumed to be ideal and a fixed parameter to ensure the full perturbation of the rest of the belt, which is theoretically estimated by (Kuchynka et al., 2010), is properly accounted for. Also estimating the ring's mass does not result in a conclusive or valuable scientific return. The ring assumes one lumped mass value for 332 non negligibly perturbing asteroids plus around 26,000 other bodies. So there is no way that one can attribute any improvements that one can see in the ring mass due to introduction of laser ranging to any of the individual asteroids in the belt. In modern ephemerides generation models, saying something about improvements in individual asteroid masses, especially those 343 non negligible ones, is what is currently considered a scientifically valuable return. Stating how much improvement laser ranging can have on belt's lumped mass in this thesis does not provide any meaningful or conclusive additions on what is happening with individual masses in the solar system. It would haven be useful to also estimate the ring mass if the 343 non-negligible asteroid masses were estimated individually. Then the ring mass would give insight on the lumped mass of the 26,000 remaining bodies in the belt which the signature of their effect are believed to be similar to one another (Kuchynka et al., 2010), allowing one to further improve the knowledge of the belt.

The correlation matrices of the estimated asteroid masses with other parameters are shown in in Figure 4.18. The inter-correlation between the asteroid masses themselves are quite high which is expected due to the effect that the asteroid masses they have on themselves and slightly similar effect signature they have on the orbit of Mars. The correlation to Mars's orbital parameters are high and are significantly elevated when laser ranging introduced which is also expected. The masses show elevated correlations to inner planets' positions as well which is due to them having non-negligible effects on orbit of Mercury and Venus too as was displayed in Figure 2.4. There are some oddly

high correlations between asteroid masses and some of Neptune's orbital parameters which could be related to bad constraints on Neptune's orbit.

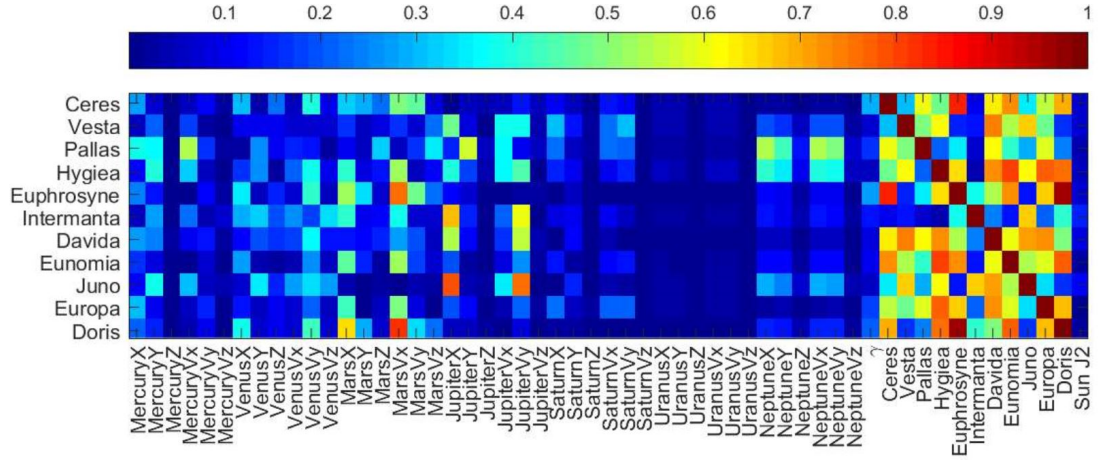

(A) Correlation of asteroid mass parameters with all 55 estimated parameters without any laser ranging data to Mars

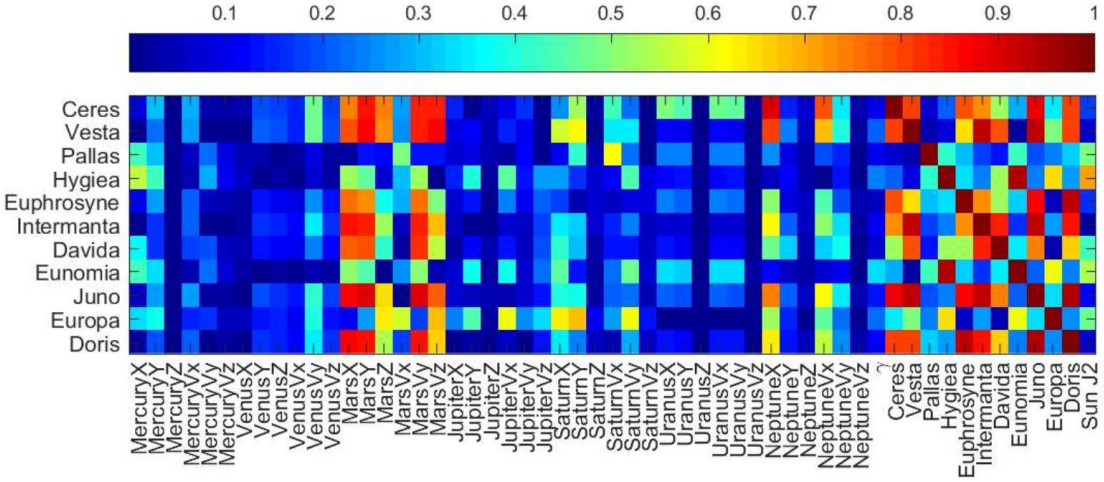

(B) Correlation of asteroid mass parameters with all 55 estimated parameters with laser ranging data to Mars

FIGURE 4.18: Comparison of asteroid mass parameters correlation with all 55 estimated parameters between the two cases of with and without laser ranging to Mars

4.3 Laser ranging effect on Sun's J2 and PPN parameter γ

Interplanetary laser ranging is a very prolific way of determining relativistic parameters that exist in the PPN formalism of the Newton's acceleration model (i.e γ and β) (Dallas, 1977). The reason for this is directly derived from the fact that laser ranging result in accurate determination of planetary state vector which in turn allows for estimating the relativistic parameters that exists in the planet's acceleration model. The estimated PPN parameter with and without laser ranging to Mars as well as its correlation with

planetary ephemerides are displayed in this Section. Table 4.2 displays the estimated γ and Sun's J_2 parameter as well as their true values which are extracted from the virtual reality model (i.e truth model). The comparison between the two values can be used to get an idea of the true error of the estimation. Next to this, the formal error of the estimation is also shown to give insight on the ratio of true to formal error.

TABLE 4.2: Estimated dynamical and relativistic parameters with and without ILR compared to their true values to get an indication of the true error of the estimation as well as the formal error of the estimation.

Parameter Name	*True value from Truth Model*	*Estimated value without ILR*	*Estimated value with ILR*	*Formal Error without ILR*	*Formal Error with ILR*
$\gamma - 1$	0.0	8.237×10^{-5}	5.5×10^{-8}	1.49×10^{-5}	7.52×10^{-8}
Sun J_2	2.0×10^{-7}	1.704×10^{-7}	1.980×10^{-7}	1.54×10^{-8}	5.48×10^{-10}

From Table 4.2, a preliminary conclusion can be made on the significance of laser ranging on testing general relativity as it is capable of reduce the uncertainty on γ from 10^{-5} level to 10^{-7}. Table 4.2 shows that the true error of the γ without laser ranging is inline what is suggested in literature and the value that was determined from the Cassini experiment (Kopeikin et al., 2007). This acts as a verification of the produced results as well as showing that the relative improvement that is seen due to laser ranging. The same goes for for the Sun's oblateness factor which also sees a great improvement which is not only due to improvement in orbit of Mars itself but also the cascade effect on laser ranging on orbit of Mercury that experiences the largest perturbation due to Sun's oblateness. Also formal errors in Table 4.2 illustrate that the formal errors are more optimistic by a factor of up to 5 compared to the the true error which was also predicted in Section 3.3 and it justifies using the systematic noise designed in Section 2.6.1 during the estimation to get more realistic representation of error.

The correlation between the PPN parameter and the other 54 estimated parameters are given in Figure 4.19 for both cases. Figure 4.20 shows the correlation of estimated Sun's oblateness parameter with the rest of the estimated parameters.

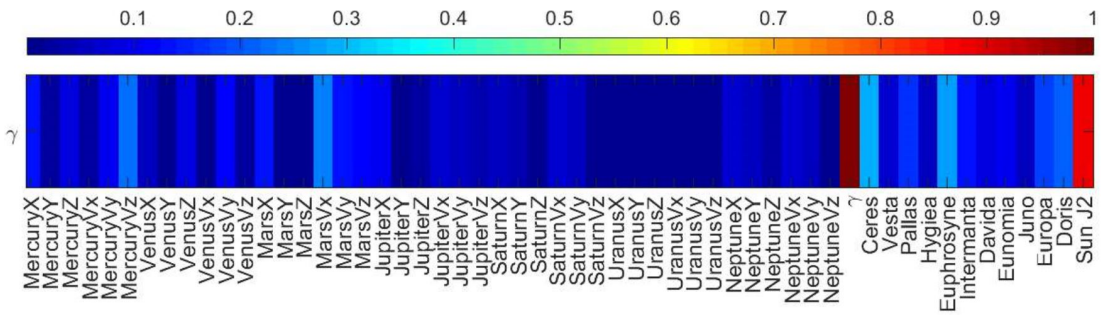

(A) Correlation of PPN parameter γ with other 54 estimated parameters without any laser ranging data to Mars

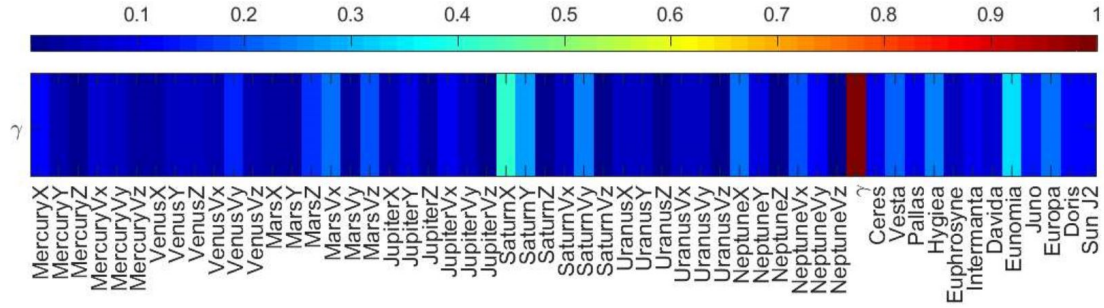

(B) Correlation of PPN parameter γ with other 54 estimated parameters with laser ranging data to Mars

FIGURE 4.19: Comparison of γ's correlation with other estimated parameters between the two cases of with and without laser ranging to Mars

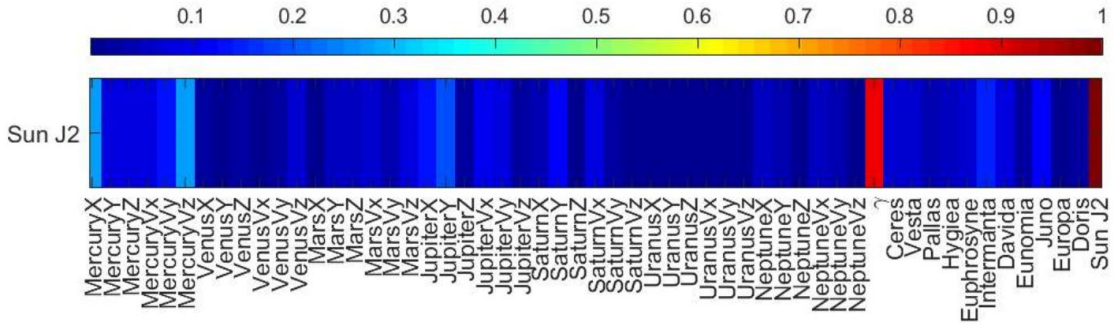

(A) Correlation of Sun's J_2 parameter with other 54 estimated parameters without any laser ranging data to Mars

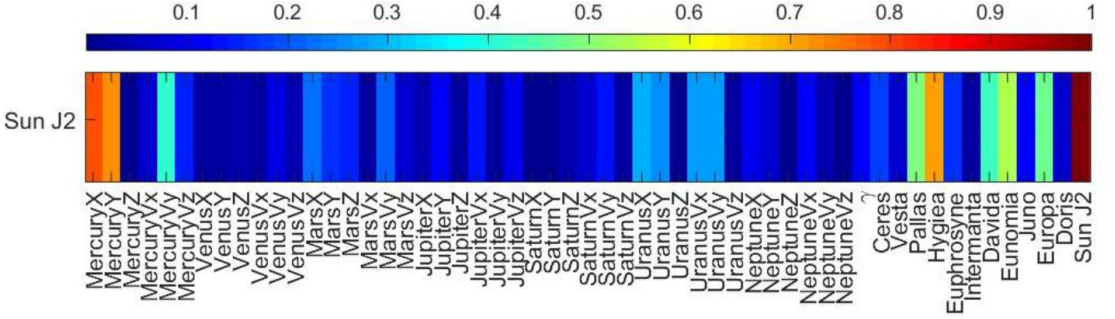

(B) Correlation of Sun's J_2 parameter with other 54 estimated parameters with any laser ranging data to Mars

FIGURE 4.20: Comparison of Sun's J_2's correlation with other estimated parameters between the two cases of with and without laser ranging to Mars

Some notable observations can be made by comparing the Figures in 4.19 and 4.20. One is that PPN parameter γ and Sun's J_2 parameter seem to display very high correlation (i.e 0.85) for the case when laser ranging is not utilized. For the case where laser ranging to Mars is utilized, these correlation disappears as very accurate observation to Mars, and in turn better determination of Mercury's orbit result allows for better distinction between the Sun's gravitational and relativistic effects. This is also helped by selecting a very small Sun avoidance angle to better distinguish the two effects. Since laser ranging observations are much more accurate, the effect is more prominently distinguished for the case where laser ranging is used, completely decorrelating these two parameters. The reason why small Sun avoidance angle did not help decorrelating the parameter for the case where laser ranging is not utilized is because the observation accuracy in that case is not good enough to properly distinguish the two effects.

Figure 4.20 shows that Sun's J_2 effect gets elevated correlation to Mercury when laser ranging introduced which is expected as Mercury is the planet that is most significantly effect of the Sun's gravitation and the more accurately it is known, the better it can be used to estimated Sun's oblateness factor. Since laser ranging also improves asteroid masses and orbital parameters of other bodies, one can see that Sun's J_2 effect on their orbit is much more accurately captured as well which is displayed by the elevated correlations.

Chapter 5

Conclusion & Recommendation

The purpose of this thesis was to illustrate the effect of interplanetary laser ranging on planetary ephemerides accuracy and answer the research questions posed in Section 1.2, specifically How much improvement in planetary ephemerides uncertainty (or error) can be achieved by introducing interplanetary laser ranging observation in a planetary ephemerides generation process. It was shown that due to dynamical coupling between the bodies in the solar system, introducing a 3 year period of laser ranging to Mars results in a more stable and more accurate planetary ephemerides. Some of this improvement in accuracy and stability is attributed to the improvement in knowledge of the asteroid masses which see up to a factor of ten improvement in their mass parameter uncertainty due to the 3 year period of laser ranging introduced to Mars as was shown in Section 4.2. Accurate laser ranging to Mars and its cascade effect on other planetary ephemerides resulted in much better determination of Sun's oblateness factor (i.e J_2) and PPN parameter γ, improving their uncertainty 2 and 3 orders of magnitude respectively as was shown in Table 4.2 of Section 4.3. The body that is the target planet of laser ranging sees a drastic improvement in its orbital uncertainty which was shown that Mars's position uncertainty improved from tens of meters level to less than a meter level accuracy during the laser ranging phase which was apparent by looking at Figure 4.10.

The results that have been produced in this thesis are based on a number of assumptions explained in Chapter 2 and are under computational limitations. Some of these main assumptions, their impact and recommendation on how to treat them in future studies are explained in the following. The simulation that is modeled in this thesis is set up in such a way that it provides a great framework to do further studies and test other hypothesis based off what was already done here. Any other analysis can be done by making use of the ephemerides generation model that was already developed in this thesis as it is designed in a way that by simple adjustments of initial inputs of the simulation, any desired analysis can be performed. That being said, a number of shortcomings that this thesis

could not address and the author suggests to be looked at in the future are provided here.

First and foremost, the ephemerides generation process have been conducted without estimating the states of Earth and Moon due to getting bad condition numbers and unreliable and diverging results as was explained in in Section 2.9. This assumption is equivalent of having very accurate apriori knowledge of these two bodies to a point where interplanetary laser ranging wont affect their orbits as much. This is of course not true and it is recommended to estimate the state of these two bodies along side with other bodies in the future estimation studies to analyze the correlation between the Earth and other states. This requires some research on how exactly Earth and Moon are treated in the state of the art ephemerides generation models and how they are constrained such that the problem does not become ill-conditioned.

The second recommendation is to estimate all 343 non negligible asteroids individually and extending the timespan of the simulation for longer periods. These two changes require immense amount of computational budget which was not available at the time when this thesis was conducted. The reason why these are recommended is that it will result in having ephemerides generation model that closely represent the state of the art ones. Also one can analyze the effect of laser ranging on individual asteroid masses which gives much more insight on how well one can improve the current knowledge of the asteroid belt from laser ranging. The reason why a wider timespan is recommended it to properly and fully carry over all the past information and planetary observations that are available to us into the estimation model which will result in a simulation that accurately represent our current knowledge of the ephemerides and subsequently the effect of laser ranging on it. For instance, similar to state of the art models, starting the estimation from 1969 onward which contains all of the most significant planetary observations which had a large effect on the current knowledge of the ephemerides. The developed code for this thesis already has the functionality implemented which allows for selection of any time span and any number of asteroids to estimate by simply adjusting its input parameters which allows performing this recommendation with minimum effort

In this thesis only the effect of laser ranging on PPN parameter γ was analyzed under the assumption that Nordtvedt parameter is equal to its nominal value which results in all relativistic effects to be represented by one parameter γ. It is recommended that a more specific analysis to be performed on the effect of laser ranging on relativistic parameters and its contribution to testing general relativity by using constraint equations during estimation in order to properly decorrelate and estimate more than one of the PPN parameters. There are already studies that have been performed to analyze the effect of laser ranging on relativistic parameters such as (Turyshev et al., 2010) which can be used as a good guideline for conducting further relativistic studies.

Finally, in this thesis only the effect of laser ranging to one target planet (i.e Mars)

was investigated as this planet was believed to be the most optimum and realistic candidate. However, this thesis can turn into an optimization problem in which one can investigate the mose cost effective and prolific target and duration for laser ranging such that one can get the most out of its benefits. This can be a great optimization problem which help with designing future interplanetary mission in order to get the most out of them. Also the code developed in this thesis can be used to test any desirable case without the requirement of having knowledge of TUDAT or C++ for that matter as all the inputs are easily adjustable.

Appendix A

Elliptical Integrals

The first, $K(k)$, and second, $E(k)$, kind of complete elliptical integrals used in this paper have the following representations (Bertoli et al., 2014)

$$K(k) = E(k, \frac{\pi}{2}) = \int_0^{\frac{\pi}{2}} \frac{1}{\sqrt{1 - k^2 sin^2 x}} dx \tag{A.1}$$

$$E(k) = E(k, \frac{\pi}{2}) = \int_0^{\frac{\pi}{2}} \sqrt{1 - k^2 sin^2 x} dx \tag{A.2}$$

With k being the elliptic modulus. The incomplete elliptical integral has boundaries between 0 and any value but the complete form, which is used in computing the ring acceleration in this paper, has boundary needs to be between 0 and $\frac{\pi}{2}$. The solution to the complete elliptical integrals for first and second kind can be represented in terms of a power series shown below (Bertoli et al., 2014)

$$K(k, \frac{\pi}{2}) = \frac{\pi}{2} \sum_{n=0}^{\infty} \left[\frac{2n! k^n}{2^{2n} n!^2} \right]^2 \tag{A.3}$$

$$E(k, \frac{\pi}{2}) = \frac{\pi}{2} \sum_{n=0}^{\infty} \left[\frac{2n! k^n}{2^{2n} n!^2} \right]^2 \left[1 - \frac{k^2}{2} - \frac{k^4}{8} \frac{(2n+1)^2}{(r+1)(r+2)} \right] \tag{A.4}$$

These power series are numerically solved for a certain number of n depending on the required numerical precision.

Appendix B

Numerical derivative

The partial derivatives of the acceleration model with respect to the estimated parameters are required to be computed to populated the state transition matrix. However the analytically deriving some of those partial derivatives can become very cumbersome to compute and implement (i.e Equation 2.12). Hence the derivative is computed numerically using the following procedure. Assuming $f(\bar{x}, t)$ is a function which its partial derivative with respect to parameter x_i needs to be computed. Then Equation B.1 is utilized which uses central differencing to numerically compute the derivative of a function (Smith, 1985).

$$\frac{df(\bar{x}, t)}{dx_i} = \frac{f(\bar{x}_{(p,+)}, t) - f(\bar{x}_{(p,-)}, t)}{2x_p} \tag{B.1}$$

With $\bar{x}_{(p)}$ representing the perturbed parameter vector $\bar{x}$ in which only one of its parameter, x_i, is perturbed. $\bar{x}_{(p,+)}$ stands for a positively perturbed i^{th} parameter and $\bar{x}_{(p,-)}$ stands for a negatively perturbed i^{th} parameter. The function is evaluated at the two perturbed instances and the average of the two are selected as the function derivative. This process is repeated for every parameter in parameter vector $\bar{x}$ that the function f is sensitive to. x_p represents the magnitude of the perturbation put on perturbed parameter x_i.

Appendix C

Parameter Estimation process

The main theoretical basis behind this thesis is the process of estimating the state of the solar system bodies. This is done using the weighted least-square parameter estimation process which aims to estimate a vector of parameters (containing bodies initial states and a number of physical and environmental parameters or observation biases that are to be estimated, such that the actual observation data fit the dynamical model of the solar system as good as possible by ensuring that the difference between the two are minimized. The state vector is shown as vector $\bar{X}$ below which contains initial positions and velocities of ith body while $\bar{p}$ contains all the additional estimated parameters.

$$\bar{S}(t) = \begin{bmatrix} \vdots \\ x_i(t) \\ y_i(t) \\ z_i(t) \\ \dot{x}_i(t) \\ \dot{y}_i(t) \\ \dot{z}_i(t) \\ \vdots \end{bmatrix} \quad \bar{X} = \begin{bmatrix} \bar{S}_0 \\ \bar{p} \end{bmatrix}$$

C.1 Inclusion of dynamics

To include dynamics in the parameter estimation process, two steps are considered. First one is integrating the equations of motion, F, in order to get states in the future(or past) epochs. F describes the rate of change of state over time is determined by the dynamical equation of motion which describes the motion of the bodies in the solar system.

$$\dot{\bar{S}}(t) = F(\bar{S}, t)$$

The second step is to implement a functionality in the parameter estimation process such that a small change in initial state translates into a change in states at any desired time. This is achieved by state transition matrix ϕ(or variational equations) which is a Jaccobian matrix of function F, evaluated at a certain reference state (i.e a matrix which each elements of it is a partial derivative of F with respect to each of the state and dynamical parameters) (Schutz et al., 2004)

$$\Delta X(t) = \phi(t, t_0)\Delta X(t_0)$$

The state transition matrix itself needs to be propagated to future epochs which is done by using a numerical integration scheme. Hence the variation of state transition matrix over time is defined as the following (Schutz et al., 2004)

$$\dot{\phi}(t, t_0) = \left.\frac{\delta F}{\delta X}\right|_{X=X_{ref}} \phi(t, t_0)$$

It is typical to divide ϕ matrix into a sensitivity matrix (i.e containing $\frac{\delta F}{\delta p}$ and another matrix (i.e containing $\frac{\delta F}{\delta S}$) which improves efficiency in practice but in this discussion, the combined matrix is used and referred to as ϕ.

C.2 Inclusion of observations and observation model

The observations data used in parameter estimation process could be range, range-rate or various angles which do not represent the actual states of the bodies. In fact, a nonlinear observation equation relate the observation to the actual states. Hence, to write the relationship between observation and observation equation in a matrix formulation, the observation equation need to be linearized around a reference state by using a first order Taylor expansion as shown below (Schutz et al., 2004). The observations are referred to as $\bar{y}$.

$$\bar{y} = \bar{y}_{ref} + \underbrace{\left.\frac{\delta \bar{y}}{\delta X}\right|_{X=X_{ref}}}_{\hat{H}} \underbrace{(X - X_{ref})}_{\Delta \mathrm{X}} + \bar{\epsilon}$$

$\bar{\epsilon}$ in this case is a vector containing observation errors (both systematic and random) and $\hat{H}$ is a matrix that maps the increment of observation to the increment of state. In least square method, the above is typically rearranged in the following form which express the increment of observation as a linear combination of design matrix A and the increments of the state vector S

$$\Delta y(t) = \hat{H}(t)\Delta X(t) + \epsilon(t)$$

Above equation can be written in terms of deviation in initial state vector (or in terms of a deviation in an state vector at time t_k) using matrix ϕ. This translate the above relation into the following form (Schutz et al., 2004)

$$\Delta y(t) = \hat{H}(t)\phi(t, t_k)\Delta X(t_k) + \epsilon(t)$$

In a weighted least square estimation problem, each observation has a weight assigned to it which all of them are gathered a weight matrix denoted as W. This matrix is derived from the observation covariance which is a representative of the observation noise. In case of uncorrelated Gaussian noise for observation, this matrix is a diagonal matrix containing $\frac{1}{\sigma^2}$ for each observation with σ^2 being the variance of the observation.

The least square inversion process involves minimizing the weighted sum squares of the calculated observation residuals (i.e difference between the actual observation and the computed one) which is denoted as the following cost function (Schutz et al., 2004)

$$J = \frac{1}{2}\epsilon^t W \epsilon$$

The assumption and conditions that are used for minimizing this function is discussed in (Schutz et al., 2004). The minimization will result in Equation C.1 which determines the best estimate for ΔX such that the weighted sum squares of the calculated observation residuals are minimized.

$$\Delta X(t_k) = (H^T(t_k) W H(t_k))^{-1} H^T(t_k) W \Delta y \tag{C.1}$$

Since this both the observation equation and the dynamic are nonlinear, a number of iterations are required until the solution can be reached. At each iteration, estimated state increment is added to the state then computed observation is compared to the actual observation. If the difference is smaller than a certain preset threshold, the iteration is stopped. If the convergence is not reached, then one shall observe and identify the source that prevents the computed values to be close the actual ones either in the observation model or the dynamic.

C.2.1 Estimation formal error

After the estimation is performed, one can extract the covariance matrix of vector X which the square root of its diagonal elements provide the formal error of the estimation process. The covariance matrix is determined as follows with P_{apr}^{-1} that is called

the a-priori covariance matrix which is constructed from the apriori knowledge of each parameter and it has the square of the standard deviation of each parameter on its diagonal (Wermuth et al., 2010).

$$P_x^{-1} = (H^T W H)^{-1} + P_{apr}^{-1}$$

Bibliography

Baer, J., Chesley, S. R., and Matson, R. D. (2011). Astrometric masses of 26 asteroids and observations on asteroid porosity. *The Astronomical Journal*, 141(5):143.

Bauer, S., Hussmann, H., Oberst, J., Dirkx, D., Mao, D., Neumann, G. A., Mazarico, E., Torrence, M., McGarry, J., Smith, D., et al. (2016). Demonstration of orbit determination for the lunar reconnaissance orbiter using one-way laser ranging data. *Planetary and Space Science*, 129:32–46.

Bertoli, S. L., Ender, L., De Almeida, J., and da Silva Kalvelage, P. M. (2014). Solutions of elliptic integrals and generalizations by means of bessel functions. *Applied Mathematics and Computation*, 243:33–43.

Cartwright, J. H. and Piro, O. (1992). The dynamics of runge–kutta methods. *International Journal of Bifurcation and Chaos*, 2(03):427–449.

Cavanaugh, J. F., Smith, J. C., Sun, X., Bartels, A. E., Ramos-Izquierdo, L., Krebs, D. J., McGarry, J. F., Trunzo, R., Novo-Gradac, A. M., Britt, J. L., et al. (2007). The mercury laser altimeter instrument for the messenger mission. *Space Science Reviews*, 131(1-4):451–479.

Dallas, S. (1977). Equations of motion for rotating finite bodies in the extended ppn formalism. *Celestial mechanics*, 15(1):111–123.

Dickey, J. O., Bender, P., Faller, J., Newhall, X., Ricklefs, R., Ries, J., Shelus, P., Veillet, C., Whipple, A., Wiant, J., et al. (1994). Lunar laser ranging: A continuing legacy of the apollo program. *Science*, 265(5171):482–490.

Dirkx, D. (2015). Interplanetary laser ranging. analysis for implementation in planetary science missions.

Dirkx, D., Vermeersen, L., Noomen, R., and Visser, P. (2014). Phobos laser ranging: Numerical geodesy experiments for martian system science. *Planetary and Space Science*, 99:84–102.

Exertier, P., Bonnefond, P., Deleflie, F., Barlier, F., Kasser, M., Biancale, R., and Ménard, Y. (2006). Contribution of laser ranging to earth's sciences. *Comptes Rendus Geoscience*, 338(14-15):958–967.

Fienga, A., Laskar, J., Kuchynka, P., Manche, H., Desvignes, G., Gastineau, M., Cognard, I., and Theureau, G. (2011). The inpop10a planetary ephemeris and its applications in fundamental physics. *Celestial Mechanics and Dynamical Astronomy*, 111(3):363.

Folkner, W. (2010). Uncertainties in the jpl planetary ephemeris. In *Proceedings of the Journées*, page 43.

Folkner, W., Iess, L., Anderson, J., Asmar, S., Buccino, D., Durante, D., Feldman, M., Gomez Casajus, L., Gregnanin, M., Milani, A., et al. (2017). Jupiter gravity field estimated from the first two juno orbits. *Geophysical Research Letters*, 44(10):4694–4700.

Folkner, W. M., Williams, J. G., Boggs, D. H., Park, R. S., and Kuchynka, P. (2014). The planetary and lunar ephemerides de430 and de431.

Genova, A., Mazarico, E., Goossens, S., Lemoine, F. G., Neumann, G. A., Smith, D. E., and Zuber, M. T. (2018). Solar system expansion and strong equivalence principle as seen by the nasa messenger mission. *Nature communications*, 9(1):289.

Helled, R., Anderson, J. D., Podolak, M., and Schubert, G. (2010). Interior models of uranus and neptune. *The Astrophysical Journal*, 726(1):15.

Hulley, G. and Pavlis, E. (2007). A ray-tracing technique for improving satellite laser ranging atmospheric delay corrections, including the effects of horizontal refractivity gradients. *Journal of Geophysical Research: Solid Earth*, 112(B6).

Konopliv, A. S., Asmar, S. W., Folkner, W. M., Karatekin, Ö., Nunes, D. C., Smrekar, S. E., Yoder, C. F., and Zuber, M. T. (2011). Mars high resolution gravity fields from mro, mars seasonal gravity, and other dynamical parameters. *Icarus*, 211(1):401–428.

Kopeikin, S. M., Polnarev, A., Schäfer, G., and Vlasov, I. Y. (2007). Gravimagnetic effect of the barycentric motion of the sun and determination of the post-newtonian parameter γ in the cassini experiment. *Physics Letters A*, 367(4-5):276–280.

Kral, L., Prochazka, I., and Hamal, K. (2005). Optical signal path delay fluctuations caused by atmospheric turbulence. *Optics letters*, 30(14):1767–1769.

Kuchynka, P. and Folkner, W. M. (2013). A new approach to determining asteroid masses from planetary range measurements. *Icarus*, 222(1):243–253.

Kuchynka, P., Laskar, J., Fienga, A., and Manche, H. (2010). A ring as a model of the main belt in planetary ephemerides. *Astronomy & Astrophysics*, 514:A96.

Lemoine, F. G., Goossens, S., Sabaka, T. J., Nicholas, J. B., Mazarico, E., Rowlands, D. D., Loomis, B. D., Chinn, D. S., Caprette, D. S., Neumann, G. A., et al. (2013). High–degree gravity models from grail primary mission data. *Journal of Geophysical Research: Planets*, 118(8):1676–1698.

Luo, Y.-z. and Yang, Z. (2017). A review of uncertainty propagation in orbital mechanics. *Progress in Aerospace Sciences*, 89:23–39.

Moyer, T. D. (2005). *Formulation for observed and computed values of Deep Space Network data types for navigation*, volume 3. John Wiley & Sons.

Neumann, G., Cavanaugh, J., Coyle, D., McGarry, J., Smith, D., Sun, X., Torrence, M., Zagwodski, T., and Zuber, M. (2006). Laser ranging at interplanetary distances. In *Proc. 15-th International Workshop on Laser Ranging, Canberra, Australia*.

Petit, G. and Luzum, B. (2010). Iers conventions (2010). Technical report, BUREAU INTERNATIONAL DES POIDS ET MESURES SEVRES (FRANCE).

Pitjeva, E. (2013). Updated iaa ras planetary ephemerides-epm2011 and their use in scientific research. *Solar System Research*, 47(5):386–402.

Plaut, J., Barabash, S., Bruzzone, L., Dougherty, M., Erd, C., Fletcher, L., Gladstone, R., Grasset, O., Gurvits, L., Hartogh, P., et al. (2014). Jupiter icy moons explorer (juice): Science objectives, mission and instruments. In *Lunar and Planetary Science Conference*, volume 45, page 2717.

Schutz, B., Tapley, B., and Born, G. H. (2004). *Statistical orbit determination*. Academic Press.

Shapiro, I., Reasenberg, R., Chandler, J., and Babcock, R. (2003). Measurement of the de sitter precession of the moon: A relativistic three-body effect. In *Nonlinear Gravitodynamics: The Lense-Thirring Effect*, pages 501–504. World Scientific.

Smith, D. E., Zuber, M. T., Sun, X., Neumann, G. A., Cavanaugh, J. F., McGarry, J. F., and Zagwodzki, T. W. (2006). Two-way laser link over interplanetary distance. *Science*, 311(5757):53–53.

Smith, G. D. (1985). *Numerical solution of partial differential equations: finite difference methods*. Oxford university press.

Standish, E. M. and Williams, J. G. Orbital ephemerides of the sun, moon, and planets.

Standish Jr, E. M. and Hellings, R. W. (1989). A determination of the masses of ceres, pallas, and vesta from their perturbations upon the orbit of mars. *Icarus*, 80(2):326–333.

Timmer, J. and Koenig, M. (1995). On generating power law noise. *Astronomy and Astrophysics*, 300:707.

Tommei, G., Milani, A., and Vokrouhlickỳ, D. (2010). Light-time computations for the bepicolombo radio science experiment. *Celestial Mechanics and Dynamical Astronomy*, 107(1-2):285–298.

Touma, J. and Wisdom, J. (1994). Evolution of the earth-moon system. *The Astronomical Journal*, 108:1943–1961.

Turyshev, S. G., Farr, W., Folkner, W. M., Girerd, A. R., Hemmati, H., Murphy, T. W., Williams, J. G., and Degnan, J. J. (2010). Advancing tests of relativistic gravity via laser ranging to phobos. *Experimental Astronomy*, 28(2-3):209–249.

Turyshev, S. G., Williams, J. G., Shao, M., Anderson, J. D., Nordtvedt Jr, K. L., and Murphy Jr, T. W. (2004). Laser ranging to the moon, mars and beyond. *arXiv preprint gr-qc/0411082*.

Verma, A., Fienga, A., Laskar, J., Manche, H., and Gastineau, M. (2014). Use of messenger radioscience data to improve planetary ephemeris and to test general relativity. *Astronomy & Astrophysics*, 561:A115.

Viswanathan, V., Fienga, A., Gastineau, M., and Laskar, J. (2017). Inpop17a planetary ephemerides. *Notes Scientifiques et Techniques de l'Institut de mécanique céleste,(ISSN 1621-3823),# 108, ISBN 2-910015-79-3, 2017, 39 pp.*, 108.

Wakker, K. F. (2015). Fundamentals of astrodynamics. *Institutional Repository Library Delft University of Technology, Delft, The Netherlands*, pages 534–537.

Wermuth, M., Montenbruck, O., and Van Helleputte, T. (2010). Gps high precision orbit determination software tools (ghost). In *Proceedings of 4th International Conference on Astrodynamics Tools and Techniques, Madrid, ESA WPP-308*, pages 3–6. Citeseer.

Williams, J. G., Turyshev, S. G., and Boggs, D. H. (2004). Progress in lunar laser ranging tests of relativistic gravity. *Physical Review Letters*, 93(26):261101.

Xie, Y. and Deng, X.-M. (2013). f (t) gravity: effects on astronomical observations and solar system experiments and upper bounds. *Monthly Notices of the Royal Astronomical Society*, 433(4):3584–3589.

Zasova, L., Ignatiev, N., Korablev, O., Eismont, N., Gerasimov, M., Khatuntsev, I., Jessup, K. L., and Economou, T. (2017). Venera-d: Expanding our horizon of terrestrial planet climate and geology through the comprehensive exploration of venus.